METHODS

Generation of Atg16L1-deficient mice. The fragment of the Atg16L1 gene was isolated from genomic DNA extracted from wild-type ES cells by PCR. A targeting vector was constructed by replacing exons 3, 4 and 5 of Atg16L1 with a neomycin-resistance gene cassette (neo), and a herpes simplex virus thymidine kinase driven by PGK promoter was inserted into the genomic fragment for negative selection. After the targeting vector was transfected into ES cells, G418 and gancyclovir doubly resistant colonies were selected and screened by PCR and Southern blotting. Homologous recombinants were micro-injected into C57BL/6 female mice, and heterozygous F1 progenies were intercrossed in order to obtain Atg16L1-deficient (Δ/Δ) mice. The Atg16L1-deficient mice used were on a 129Sv × C57BL/6 background.

For the generation of fetal liver chimaeric mice, fetal liver cells were harvested at E15.5 and injected into lethally irradiated CD45.1 or C57BL6J mice. Chimaeric mice were given antibiotics in drinking water for 2 months. The mice were analysed at least 3 months after reconstitution.

Mice were maintained in our animal facility and treated in accordance with the guidelines of Osaka University.

Reagents, mice and cells. Anti-IL-1β antibodies, recombinant mouse IFN-γ, ELISA kits for mouse IL-1β, human IL-1β, mouse IL-6 and mouse TNFα, were purchased from R&D Systems. Recombinant mouse IFN-β and the ELISA kit for mouse IFN-β were purchased from PBL InterferonSource. Anti-LC3 and anti-IL-18 antibodies and the ELISA kit for IL-18 were purchased from MBL International. GM-CSF and M-CSF were purchased from Peprotech. Anti-p62/SQSTM1 antibody was purchased from BIOMOL International. Anti-Atg12, anti-phospho-IRF3, anti-phospho-p38 and anti-phospho-ERK antibodies were purchased from Cell Signaling Technology. Anti-IκBα, anti-ERK and caspase-1 p10 were purchased from Santa Cruz Biotechnology. YVAD-fmk, wortmannin and FeTPPS were purchased from Calbiochem. ATP, oxidized ATP, LPS from *Salmonella minnesota* Re 595, 3-methyadenine, muramyl dipeptide and anti-α-tubulin antibody were purchased from Sigma. Lipid A was purchased from Peptide Institute. Flagellin was purchased from Invivogen. Uric acid crystals were purchased from Alexis. N-acetyl-L-cysteine was purchased from Nacalai Tesque. Poly(I)·poly(C) was purchased from GE Healthcare. R-848 was kindly provided by the Pharmaceuticals and Biotechnology Laboratory Japan Energy Corporation. CpG oligodeoxynucleotides (ODN1668) were synthesized at Hokkaido System Science Co. Anti-Atg16L1and anti-Atg5 antibodies were kindly donated by N. Mizushima (Tokyo Medical and Dental University).

K. pneumonia and *E. aerogenes* were kindly donated by the Research Institute of Microbial Disease, Osaka University. *E. coli* (DH5α) was purchased from TOYOBO. *Salmonella enteritica serovar typhimurium* (SR-11 × 3181) was provided by the Kitasato Institute for Life Science. Mice deficient in MyD88, TRIF or Atg7 were described previously[9,13]. Atg5-deficient MEFs and Plat-E cells were kindly donated by N. Mizushima and T. Kitamura (University of Tokyo), respectively. RAW264.7 cells were purchased from ATCC.

Plasmids. The retroviral expression constructs pMRX-ires-puro, pMRX-ires-bsr and pMRX-ires-EGFP (donated by S. Yamaoka) were derivatives of pMX (donated by T. Kitamura). Complementary DNA encoding human IL-1β was inserted into pMRX-ires-EGFP, generating pMRX-ires-IL-1β. Complementary DNA encoding Atg16L1 lacking in coiled-coil domain (Atg16L1 ΔCCDβ) was inserted into pMRX-ires-puro, generating pMRX-Atg16L1 ΔCCDβ-ires-puro. Complementary DNA encoding the GFP-Atg5 chimaeric protein was inserted into pMRX-ires-bsr, generating pMRX-GFP-Atg5-ires-bsr. Construction and inhibitory function details of pStrawberry-Atg4^{C74A} are described elsewhere[31].

RT–PCR. Total RNA was isolated using RNAeasy Mini kits (Qiagen) according to the manufacturer's instructions. Reverse transcription was performed using ReverTra Ace (TOYOBO) according to the manufacturer's instructions. For quantitative PCR, cDNA fragments were amplified by RealTime PCR Master Mix (TOYOBO) according to the manufacturer's instructions. Fluorescence from the Taqman probe for each cytokine was detected by a 7500 Real-Time PCR System (Applied Biosystems). To determine the relative induction of cytokine mRNA in response to LPS stimulation, the mRNA expression level of each cytokine was normalized to the expression level of 18S RNA. The experiments were repeated at least twice. The results were reproducible.

The primer pairs used in Supplementary Fig. 1 are as follows. Primer pair A (exon 1-2), 5′-GTTCGGCATGTCGTCGGGCCTG-3′ and 5′-ATTTCATGCC-TATTTGGCATGTCATGC-3′. Primer pair B (exon 6-7), 5′-GTCAAGCACG-GCTGCAGAAGGAGCTTG-3′ and 5′-GTAGCTGCTCTGCTGACAGCTCGG-3′. Primer pair C (exon 1-5), 5′-GTTCGGCATGTCGTCGGGCCTGN-3′ and 5′-GACCAGTTCCTGGTTCTCCTCAGTAG-3′. Primer pair D (exon 5-7), 5′-CGCCTCAATGCAGAGAATGAGAAGGAC-3′ and 5′-GTAGCTGCTCTGCT-GACAGCTCGG-3′. Primer pair E (exon 1-6), 5′-GTTCGGCATGTCGTCG-GGCCTG-3′ and 5′-CAAGCTCCTTCTGCAGCCGTGCTTGAC-3′.

Bulk protein degradation assay. Cells were exchanged into labelling medium containing ^{14}C-valine (1.5 μCi ml^{-1}) and incubated overnight. Cells were exchanged into chase medium (DMEM supplemented with 10% FBS and 10 mM unlabelled valine) and further incubated for 4 h to remove the contribution of short-lived proteins. After the chase period, cells were exchanged into HBSS containing 10 mM valine to induce autophagy. After a 2 h incubation, the media were collected and the trichloroacetic acid (TCA)-soluble fraction was analysed by scintillation counting. Cells were lysed in ice-cold RIPA buffer and the TCA-insoluble fraction was isolated and analysed by scintillation counting. To determine the rate of long-lived protein degradation, the count in the TCA-soluble fraction in the medium was divided by the equivalent TCA-insoluble count in the cell.

Detection of apoptosis. The appearance of mono/oligo-nucleosomes, markers for apoptosis, was detected by Cell Death Detection ELISA^{PLUS} (Roche). Chromatin condensation in apoptotic nuclei was detected using an ApoStrand ELISA Apoptosis Detection Kit (Biomol). The experiments were repeated twice, and the results were reproducible.

Determination of bacteria colony forming units (c.f.u.s). Levels of c.f.u.s in freshly isolated faeces or spleen were determined by homogenization of material in PBS/0.01% Triton X-100 followed by serial dilution plating on non-selective Luria-Bertani agar.

31. Fujita, N. *et al.* An Atg4B mutant hampers the lipidation of LC3 paralogues and causes defects in autophagosome closure. *Mol. Biol. Cell* advance online publication, doi:10.1091/mbc.E08-03-0312 (3 September 2008).

Fluorophore Labeling Enables Imaging and Evaluation of Specific CXCR4–Ligand Interaction at the Cell Membrane for Fluorescence-Based Screening

Wataru Nomura,[†] Yasuaki Tanabe,[†] Hiroshi Tsutsumi,[†] Tomohiro Tanaka,[†] Kenji Ohba,[‡] Naoki Yamamoto,[‡] and Hirokazu Tamamura*,[†]

Institute of Biomaterials and Bioengineering, Tokyo Medical and Dental University, Chiyoda-ku, Tokyo 101-0062, Japan, and AIDS Research Center, National Institute of Infectious Diseases, Shinjuku-ku, Tokyo 162-8640, Japan. Received May 24, 2008; Revised Manuscript Received July 23, 2008

Development of CXCR4-specific ligands is an important issue in chemotherapy of HIV infection, cancer metastasis, and rheumatoid arthritis, and numerous potential ligands have been developed to date. However, it is difficult to assess their binding mode and specificity because of uncertainties in the structure of the CXCR4–ligand complexes. To address this problem, we have synthesized fluorophore labeled Ac-TZ14011, which is derived from T140, a powerful CXCR4 antagonist. Binding of Ac-TZ14011 to CXCR4 on the cell membrane was observed by fluorescence microscope, and analysis of the binding data produced IC_{50} values of several ligands comparable to those obtained in RI-based assays. This fluorescence-based assay is applicable to explore new pharmacophores of CXCR4-specific ligands with high-throughput screening and also to screening of the other GPCR binding ligands.

The interaction of CXCR4 with ligands causes diverse effects on cellular functions such as metastasis of progenitor cells (*1*–*3*), and a major role of CXCR4 is as the receptor of the chemokine, CXCL12. The interaction of CXCL12 with CXCR4 has been shown to be correlated with cancer progression (*4*) and $CD4^+$ T cell accumulation in the rheumatoid arthritis synovium (*5*). CXCR4 is also known as the second receptor of X4-type HIV-1 (*6*), and numerous ligands for CXCR4 derived from natural and synthetic compounds have been identified as inhibitors of HIV infection and cancer metastasis. [^{125}I]-CXCL12 has been utilized as a competitor in the assays to evaluate the CXCR4-binding activity of synthetic compounds such as T140 (*7*), its derivatives (*8*), KRH-1636 (*9*), and AMD3100 (*10*). Experimental methods utilizing radioisotopes (RI[1]) have advantages in the high resolution of the assays. Recently, molecular probes and fluorescent labeling, an emergent technology in chemical biology, have proved to be very useful for the evaluation in vivo of the functions of proteins and of the biological effect of changing concentrations of Ca^{2+} (*11*), Zn^{2+} (*12*), and NO (*13*), enzyme activity (*14*), and protein phosphorylation (*15*) in cells. Moreover, imaging of living cells by fluorescent probes can be utilized to estimate the accuracy of binding assays under statistically identical conditions. This article describes the synthesis and use of fluorophore labeled Ac-TZ14011 to analyze the CXCR4 binding of ligands at the cell membrane and to determine the IC_{50} values of ligands.

Ac-TZ14011, a derivative of T140 optimized for CXCR4 binding and stability in vivo by functional group substitutions, was synthesized as described previously (*16, 17*). The D-lysine at position 8 was selectively labeled with TAMRA or fluorescein (Figure 1). A hexamethylene group was incorporated into the TAMRA or fluorescein derivative to maintain an appropriate distance between T140 residues and the fluorophore. Residues critical to the CXCR4 binding activity of TZ14011 are Arg2, Nal3, Tyr5, and Arg14, and were assessed by screening of amino acid substitution of T140 (*16*). On the basis of the previously determined interaction between Ac-TZ14011 and CXCR4 (*18*), the fluorophores labeled at D-lysine 8 were assumed not to inhibit binding of fluorescent-Ac-TZ14011 to CXCR4. To investigate if fluorescent labeled Ac-TZ14011 maintains binding activity against CXCR4, the IC_{50} values of peptides were estimated by competitive assays against [^{125}I]-CXCL12 binding. In this assay, the IC_{50} of T140 was 3.7 nM. The IC_{50} values for fluorescein- or TAMRA-labeled Ac-TZ14011 were 11 and 14 nM, respectively. These values indicated that fluorophore labeling does not inhibit binding of Ac-TZ14011 as reported elsewhere about binding of TAMRA-Ac-TZ14011 (*19*).

The binding of TAMRA-Ac-TZ14011 to a cell membrane was observed with a laser-scanning confocal microscope to determine the specific binding of Ac-TZ14011 to CXCR4. The CXCR4-GFP fusion protein was stably expressed in the NP-2 cell line (*20*), and TAMRA-Ac-TZ14011 binding to CXCR4 was clearly observed at the membrane in the absence of competitors (Figure 2A). To assess the specific binding of ligands, excess unlabeled Ac-TZ14011 was added to the medium with TAMRA-Ac-TZ14011. Upon addition of Ac-TZ14011, weak fluorescence intensity was observed on the cell membrane or cytoplasm (Figure 2B). Vesicles observed in the cytoplasm show internalization of CXCR4 receptors induced by binding of the ligands, and signals from GFP and TAMRA showed colocalization in the cytoplasm. These results indicate the specific binding of TAMRA-Ac-TZ14011 to CXCR4. To evaluate the binding specificity for CXCR4 across the different kinds of GPCRs, HeLa cells, which stably express CD4-CCR5, were utilized for microscopy assays. The binding of TAMRA-Ac-TZ14011 was observed as for the NP-2 CXCR4-GFP cell line (Figure 2C). With the addition of excess CXCL12 (Figure

* To whom correspondence should be addressed. E-mail: tamamura.mr@tmd.ac.jp.
[†] Tokyo Medical and Dental University.
[‡] National Institute of Infectious Diseases.

[1] Abbreviations: Ac, acetyl; Cit, L-citrulline; DIC, differential interference contrast; ESI-MS, electron spray ionization-mass spectrometry; FBS, fetal bovine serum; Fmoc, 9-fluorenylmethoxycarbonyl; GPCR, G-protein-coupled receptor; HEPES, 4-(2-hydroxyethyl)-1-piperazineethanesulfonic acid; Nal, L-3-(2-naphthyl)alanine; Nal(1), L-3-(1-naphthyl)alanine; RI, radioisotope; RP-HPLC, reverse-phase HPLC; TAMRA, tetramethylrhodamine; TFA, trifluoroacetic acid.

10.1021/bc800216p CCC: $40.75
Published on Web 08/16/2008

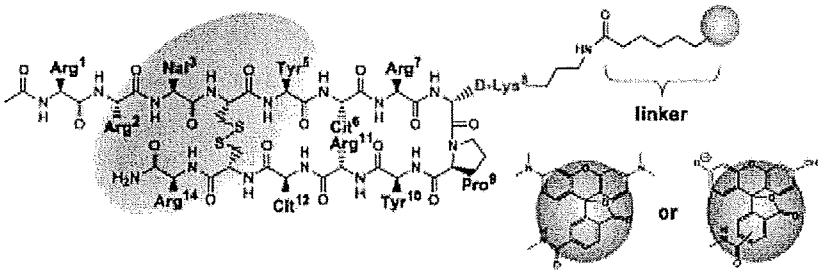

Figure 1. Design of fluorophore-labeled Ac-TZ14011. The amino acid residues in the red area are critical to CXCR4 binding activity. Fluorophores are shown as blue spheres.

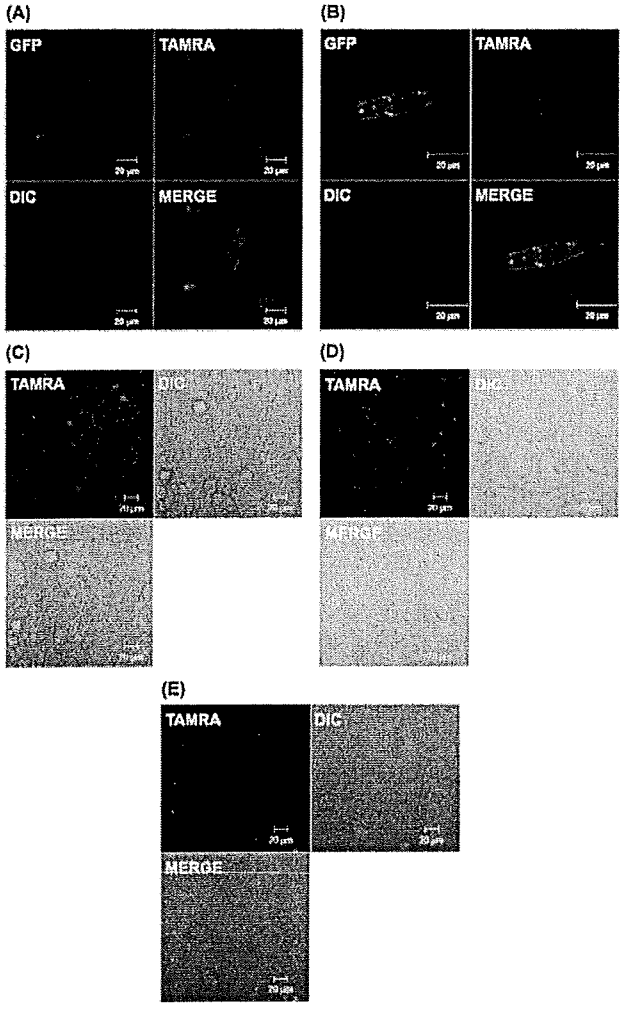

Figure 2. Confocal microscopy assays of TAMRA-Ac-TZ14011 binding to CXCR4. The signals of GFP and TAMRA are displayed in green and red, respectively. (A) Binding to NP2-GFP-CXCR4 cells. (B) Competitive binding to NP2 cells with excess amount of Ac-TZ14011. (C) Binding to HeLa-CD4-CCR5 cells. (D) Competitive binding to HeLa-CD4-CCR5 cells with excess CXCL12. (E) Competitive binding to HeLa-CD4-CCR5 cells with excess Ac-TZ14011. Descriptions of images are indicated in the pictures.

2D) or Ac-TZ14011 (Figure 2E), the fluorescence intensity on the cell membrane was decreased. These results show that TAMRA-Ac-TZ14011 binds specifically to CXCR4 but not to CCR5.

To investigate the utility of fluorescein-labeled Ac-TZ14011, cell-based binding assays were performed. In this binding assay, fluorescein-Ac-TZ14011 was utilized as a competitor to derivatives of FC131 (*8*) and the dipicolylamine-*p*-xylene Zn(II)

Table 1. K_d Values Determined by RI-Competition and Fluorescent Probe Competition Assays

	IC_{50} (nM)		
	[^{125}I]-CXCL12 competition ($IC_{50}C$)	fluorescein-Ac-TZ14011 competition ($IC_{50}F$)	$IC_{50}F/IC_{50}C$
T140	3.93	24.7	6.3
Zn^{2+}-(Dpa)-*p*-Xyl	47[a]	291	6.2
FC131	14.6	109	7.5

[a] This value is derived from ref *18*.

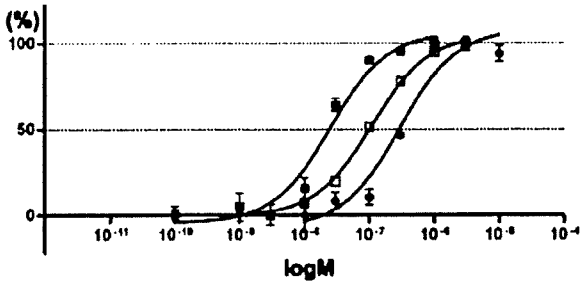

Figure 3. Curve fitting for CXCR4 binding of T140 (■), Zn^{2+}-(Dpa)-*p*-Xyl (●), and FC131 (□) in competitive assays by fluorescein-Ac-TZ14011. The *x* and *y* axes show concentrations and inhibition percentages of the binding of test compounds, respectively.

complex [Zn^{2+}-(Dpa)-*p*-Xyl] that were developed as CXCR4 antagonists (Figure 3) (*21*). The binding constants of these compounds were previously estimated by competitive assays with [^{125}I]-CXCL12. As a result, larger values of IC_{50} than those in the previous assays were observed (Table 1). The difference of the binding constants of competitors was assumed to be a reflection of the difference of IC_{50} values in the assays. It is especially interesting that the values of IC_{50} as determined by fluorescent- and RI-competition assays are clearly correlated. It was clearly indicated that binding activity of compounds can be estimated by binding inhibition assays conducted at a constant concentration of compounds. Indeed, in the detailed binding assays, a significant correlation was observed in IC_{50} values measured by both methods for T140, TC13, and TC22.

In the application of high-throughput screening for pharmacophores of CXCR4 ligands, it is important to be able to rapidly determine IC_{50} values. To test whether fluorescein-Ac-TZ14011 could be useful as a ligand in high-throughput screening, binding inhibition analyses at constant compound concentrations were performed. Twenty-four derivatives of a cyclic pentapeptide, FC131, were prepared for the analyses as described previously (Figure 4A) (*8*). The conditions used were the same as in the binding experiments shown in Figure 3 except that the compound concentration was kept constant at 2 μM. Nine compounds were found to induce >75% inhibition at this concentration (Figure 4B). The IC_{50} values of compounds that showed high inhibitory scores in the screening analyses were examined

(A)

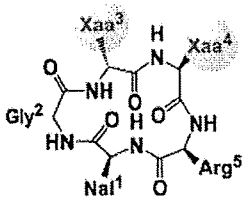

compound	Xaa^3	Xaa^4	compound	Xaa^3	Xaa^4
1	Arg	Nal	13	Arg	D-Nal
2	Nal	Arg	14	Nal	D-Arg
3	Arg	Trp	15	Arg	D-Trp
4	Trp	Arg	16	Trp	D-Arg
5	Arg	Nal(1)	17	Arg	D-Nal(1)
6	Nal(1)	Arg	18	Nal(1)	D-Arg
7	D-Arg	Nal(1)	19	D-Arg	D-Nal
8	D-Nal	Arg	20	D-Nal	D-Arg
9	D-Arg	Trp	21	D-Arg	D-Trp
10	D-Trp	Arg	22	D-Trp	D-Arg
11	D-Arg	Nal(1)	23	D-Arg	D-Nal(1)
12	D-Nal(1)	Arg	24	D-Nal(1)	D-Arg

(B)

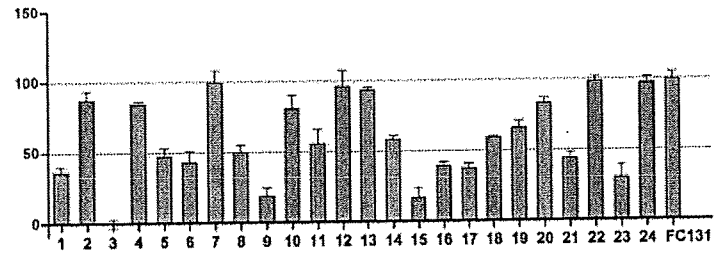

(C)

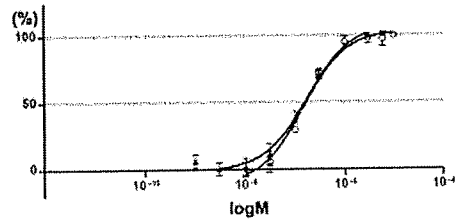

(D)

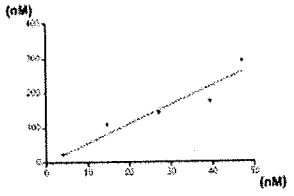

Figure 4. (A) Design of cyclic pentapeptides. Xaa^3 and Xaa^4 (red area) were manually randomized. (B) Results of single concentration point assays for determination of the binding activity of library compounds at one time. The *x* and *y* axes show concentrations and inhibition percentages of binding of test compounds, respectively. Data were measured in triplicate, and error bars show the SEM. (C) Curve fitting for CXCR4 binding of TC13 (O) and TC22 (▲) in competitive assays by fluorescein-Ac-TZ14011. The *x* and *y* axes show concentrations and inhibition percentages of binding of test compounds, respectively. (D) Correlation between IC_{50} values determined by RI-competition assays (*x*-axis) and fluorescein-Ac-TZ14011 competition assays (*y*-axis). The compound and IC_{50} values are shown in Tables 1 and 2. The *P* value determined from correlation analysis was 0.012.

Table 2. K_d Values Determined by RI-Competition and Fluorescent Probe Competition Assays

	IC_{50} (nM)		
	[^{125}I]-CXCL12 competition ($IC_{50}C$)	fluorescein-Ac-TZ14011 competition ($IC_{50}F$)	$IC_{50}F/IC_{50}C$
T140	3.93	24.7	6.3
TC13	27.0	143	5.3
TC22	39.4	176	4.5

further (Table 2). The IC_{50} values of TC13 and TC22 were determined to be 143 and 176 nM, respectively (Figure 4C). The IC_{50} values determined in this assay showed a clear correlation with those in RI-competition assays (Figure 4D, manuscript in preparation).

Advantages of the fluorescence-based analyses include their utility in high-throughput screening and direct observation of the binding state on cell membrane by fluorescence microscope; binding assays and confocal microscopy study were performed to evaluate these advantages. The binding of T140 was previously assessed with site-directed mutagenesis of CXCR4, which indicated that the extracellular loop 2 of the receptor is the main target for this peptide (*22*). The observation of Ac-TZ14011 binding to cell membranes provided convincing evidence of specificity for the target receptor. Competition with excess unlabeled Ac-TZ14011 and CXCL12 showed clear inhibition of TAMRA-Ac-TZ14011 binding. There has been concern that CXCR4 ligands could bind nonspecifically to other GPCRs. A binding study utilizing CCR5-CD4-HeLa cells showed evidence of a high degree of specificity of the ligands. HeLa cells naturally express CXCR4 (*23*), and in the event of overexpression of CCR5-CD4 on the membrane, the binding of TAMRA-Ac-TZ14011 was prevented by the addition of competitors. These results indicate that these peptides bind to the same target site on the cell membrane, CXCR4. Internalization of CXCR4 stimulated by binding of ligands was clearly observed, particularly in the presence of competitors indicating that ligands bound to CXCR4 are simultaneously incorporated in the cytoplasm. Interestingly, on the basis of the numbers and size of vesicles observed, CXCL12 showed stronger induction of CXCR4 internalization than Ac-TZ14011. Promotion of CXCR4 internalization is one of the important mechanisms for inhibition of HIV entry (*24*). The difference of ligand-dependent effects on CXCR4 internalization will be studied further in our laboratory.

In conclusion, the structure—activity relationships of ligands for CXCR4 have been well studied, but relatively few known ligand pharmacophores have been studied because of the difficulty associated with the analysis of receptor—ligand interactions. Our results strongly indicate that fluorescence-based ligand binding assays could be useful in the exploration of novel pharmacophores for CXCR4 ligands and that such compounds have promise as therapeutic agents for AIDS, breast cancer metastasis, and rheumatoid arthritis. Furthermore, this methodology is applicable to the design of ligands for other GPCRs.

ACKNOWLEDGMENT

We are grateful to Professor Kazunari Akiyoshi for his generous cooperation in experiments. This research was supported in part by a Grant-in-Aid for Scientific Research from the Ministry of Education, Culture, Sports, Science and Technology, Japan, and Health and Labour Sciences Research Grants.

Supporting Information Available: Detailed materials and methods. This material is available free of charge via the Internet at http://pubs.acs.org.

LITERATURE CITED

(1) Oberlin, E., Amara, A., Bachelerie, F., Bessia, C., Virelizier, J. L., Arenzana-Seisdedos, F., Schwartz, O., Heard, J. M., Clark-Lewis, I., Legler, D. F., Loetscher, M., Baggiolini, M., and Moser, B. (1996) The CXC chemokine SDF-1 is the ligand for LESTR/fusin and prevents infection by T-cell-line-adapted HIV-1. *Nature 382*, 833–835.

(2) Bleul, C. C., Farzan, M., Choe, H., Parolin, C., Clark-Lewis, I., Sodroski, J., and Springer, T. A. (1996) The lymphocyte chemoattractant SDF-1 is a ligand for LESTR/fusin and blocks HIV-1 entry. *Nature 382*, 829–833.

(3) Baird, A. M., Gerstein, R. M., and Berg, L. J. (1999) The role of cytokine receptor signaling in lymphocyte development. *Curr. Opin. Immunol. 11*, 157–166.

(4) Koshiba, T., Hosotani, R., Miyamoto, Y., Ida, J., Tsuji, S., Nakajima, S., Kawaguchi, M., Kobayashi, H., Doi, R., Hori, T., Fujii, N., and Imamura, M. (2000) Expression of stromal cell-derived factor 1 and CXCR4 ligand receptor system in pancreatic cancer: a possible role for tumor progression. *Clin. Cancer Res. 6*, 3530–3535.

(5) Nanki, T., Hayashida, K., El-Gabalawy, H. S., Suson, S., Shi, K., Girschick, H. J., Yavuz, S., and Lipsky, P. E. (2000) Stromal cell-derived factor-1-CXC chemokine receptor 4 interactions play a central role in $CD4^+$ T cell accumulation in rheumatoid arthritis synovium. *J. Immunol. 165*, 6590–6598.

(6) Feng, Y., Broder, C. C., Kennedy, P. E., and Berger, E. A. (1996) HIV-1 entry cofactor: functional cDNA cloning of a seven-transmembrane, G protein-coupled receptor. *Science 272*, 872–7.

(7) Tamamura, H., Xu, Y., Hattori, T., Zhang, X., Arakaki, R., Kanbara, K., Omagari, A., Otaka, A., Ibuka, T., Yamamoto, N., Nakashima, H., and Fujii, N. (1998) A low-molecular-weight inhibitor against the chemokine receptor CXCR4: a strong anti-HIV peptide T140. *Biochem. Biophys. Res. Commun. 25*, 877–882.

(8) Fujii, N., Oishi, S., Hiramatsu, K., Araki, T., Ueda, S., Tamamura, H., Otaka, A., Kusano, S., Terakubo, S., Nakanishi, H., Broach, J. A., Trent, J. O., Wang, Z., and Peiper, S. C. (2003) Molecular-size reduction of a potent CXCR4-chemokine antagonist using orthogonal combination of conformation- and sequence-based libraries. *Angew. Chem., Int. Ed. 42*, 3251–3.

(9) Ichiyama, K., Yokoyama-Kumakura, S., Tanaka, Y., Tanaka, R., Hirose, K., Bannai, K., Edamatsu, T., Yanaka, M., Niitani, Y., Miyano-Kurosaki, N., Takaku, H., Koyanagi, Y., and Yamamoto, N. (2003) A duodenally absorbable CXC chemokine receptor 4 antagonist, KRH-1636, exhibits a potent and selective anti-HIV-1 activity. *Proc. Natl. Acad. Sci. U.S.A. 100*, 4185–4190.

(10) Donzella, G. A., Schols, D., Lin, S. W., Esté, J. A., Nagashima, K. A., Allaway, G. P., Sakmar, T. P., Henson, G., De Clercq, E., and Moore, J. P. (1998) AMD3100, a small molecule inhibitor of HIV-1 entry via the CXCR4 co-receptor. *Nat. Med. 4*, 72–77.

(11) Grynkiewicz, G., Poenie, M., and Tsien, R. Y. (1985) A new generation of Ca^{2+} indicators with greatly improved fluorescence properties. *J. Biol. Chem. 260*, 3440–3450.

(12) Kiyose, K., Kojima, H., Urano, Y., and Nagano, T. (2006) Development of a ratiometric fluorescent zinc ion probe in near-infrared region, based on tricarbocyanine chromophore. *J. Am. Chem. Soc. 128*, 6548–6549.

(13) Takakusa, H., Kikuchi, K., Urano, Y., Sakamoto, S., Yamaguchi, K., and Nagano, T. (2002) Design and synthesis of an enzyme-cleavable sensor molecule for phosphodiesterase activity based on fluorescence resonance energy transfer. *J. Am. Chem. Soc. 124*, 1653–1657.

(14) Kojima, H., Urano, Y., Kikuchi, K., Higuchi, T., Hirata, Y., and Nagano, T. (1999) Fluorescent indicators for imaging nitric oxide production. *Angew. Chem., Int. Ed. 38*, 3209–3212.

(15) Ojida, A., Mito-oka, Y., Sada, K., and Hamachi, I. (2004) Molecular recognition and fluorescence sensing of monophosphorylated peptides in aqueous solution by bis(zinc(II)-dipicolylamine)-based artificial receptors. *J. Am. Chem. Soc. 126*, 2454–2463.

(16) Tamamura, H., Omagari, A., Oishi, S., Kanamoto, T., Yamamoto, N., Peiper, S. C., Nakashima, H., Otaka, A., and Fujii, N. (2000) Pharmacophore identification of a specific CXCR4 inhibitor, T140, leads to development of effective anti-HIV agents with very high selectivity indexes. *Bioorg. Med. Chem. Lett. 10*, 2633–2637.

(17) Tamamura, H., Hiramatsu, K., Mizumoto, M., Ueda, S., Kusano, S., Terakubo, S., Akamatsu, M., Yamamoto, N., Trent, J. O., Wang, Z., Peiper, S. C., Nakashima, H., Otaka, A., and Fujii, N. (2003) Enhancement of the T140-based pharmacophores leads to the development of more potent and bio-stable CXCR4 antagonists. *Org. Biomol. Chem. 1*, 3663–3669.

(18) Hanaoka, H., Mukai, T., Tamamura, H., Mori, T., Ishinoa, S., Ogawa, K., Iida, Y., Doi, R., Fujii, N., and Saji, H. (2006) Development of a 111In-labeled peptide derivative targeting a chemokine receptor, CXCR4, for imaging tumors. *Nucl. Med. Biol. 33*, 489–494.

(19) Oishi, S., Masuda, R., Evans, B., Ueda, S., Goto, Y., Ohno, H., Hirasawa, A., Tsujimoto, G., Wang, Z., Peiper, S. C., Naito, T., Kodama, E., Matsuoka, M., and Fujii, N. (2008) Synthesis and application of fluorescein- and biotin-labeled molecular probes for the chemokine receptor CXCR4. *ChemBioChem 9*, 1154–1158.

(20) Futahashi, Y., Komano, J., Urano, E., Aoki, T., Hamatake, M., Yoshida, T., Koyanagi, Y., Matsuda, Z., and Yamamoto, N. (2007) Separate elements are required for ligand-dependent and -independent internalization of metastatic potentiator CXCR4. *Cancer Sci. 98*, 373–379.

(21) Tamamura, H., Ojida, A., Ogawa, T., Tsutsumi, H., Masuno, H., Nakashima, H., Yamamoto, N., Hamachi, I., and Fujii, N. (2006) Identification of a new class of low molecular weight antagonists against the chemokine receptor CXCR4 having the dipicolylamine-zinc(II) complex structure. *J. Med. Chem. 49*, 3412–3415.

(22) Trent, J. O., Wang, Z., Murray, J. L., Shao, W., Tamamura, H., Fujii, N., and Peiper, S. C. (2003) Lipid bilayer simulations of CXCR4 with inverse agonists and weak partial agonists. *J. Biol. Chem. 278*, 47136–47144.

(23) Valente, S. T., Chanel, C., Dumonceaux, J., Olivier, R., Marullo, S., Briand, P., and Hazan, U. (2001) CXCR4 is down-regulated in cells infected with the CD4-independent X4 human immunodeficiency virus type 1 isolate m7NDK. *J. Virol. 75*, 439–447.

(24) Orsini, M. J., Parent, J. L., Mundell, S. J., Marchese, A., and Benovic, J. L. (1999) Trafficking of the HIV coreceptor CXCR4. Role of arrestins and identification of residues in the C-terminal tail that mediate receptor internalization. *J. Biol. Chem. 274*, 31076–31086.

BC800216P

A New Humanized Mouse Model of Epstein-Barr Virus Infection That Reproduces Persistent Infection, Lymphoproliferative Disorder, and Cell-Mediated and Humoral Immune Responses

Misako Yajima,[1,a] Ken-Ichi Imadome,[1,a] Atsuko Nakagawa,[2] Satoru Watanabe,[3] Kazuo Terashima,[4] Hiroyuki Nakamura,[1] Mamoru Ito,[6] Norio Shimizu,[3] Mitsuo Honda,[5] Naoki Yamamoto,[4,5] and Shigeyoshi Fujiwara[1]

[1]Department of Infectious Diseases, National Research Institute for Child Health and Development, [2]Pathology Laboratory, Department of Clinical Laboratory Medicine, National Center for Child Health and Development, [3]Department of Virology, Division of Medical Science, Medical Research Institute, and [4]Department of Molecular Virology, Graduate School of Medicine, Tokyo Medical and Dental University, and [5]AIDS Research Center, National Institute of Infectious Diseases, Tokyo, and [6]Central Institute for Experimental Animals, Kawasaki, Japan

The functional human immune system, including T, B, and natural killer lymphocytes, is reconstituted in NOD/Shi-*scid*/IL-2Rγ^{null} (NOG) mice that receive hematopoietic stem cell transplants. Here, we show that these humanized mice can recapitulate key aspects of Epstein-Barr virus (EBV) infection in humans. Inoculation with $\sim 1 \times 10^3$ TD_{50} (50% transforming dose) of EBV caused B cell lymphoproliferative disorder, with histopathological findings and latent EBV gene expression remarkably similar to that in immunocompromised patients. Inoculation with a low dose of virus ($\leqq 1 \times 10^1$ TD_{50}), in contrast, resulted in apparently asymptomatic persistent infection. Levels of activated $CD8^+$ T cells increased dramatically in the peripheral blood of infected mice, and enzyme-linked immunospot assay and flow cytometry demonstrated an EBV-specific T cell response. Immunoglobulin M antibody specific to the EBV-encoded protein BFRF3 was detected in serum from infected mice. The NOG mouse is the most comprehensive small-animal model of EBV infection described to date and should facilitate studies of the pathogenesis, prevention, and treatment of EBV infection.

Epstein-Barr virus (EBV) is a tumor virus associated with a variety of malignancies, including Burkitt lymphoma, nasopharyngeal carcinoma, and Hodgkin lymphoma [1]. It is also an etiological agent of infectious mononucleosis (IM), which is characterized by transient proliferation of EBV-infected B lymphoblastoid cells and an excessive anti-EBV T cell response. EBV has a unique ability to growth transform human B lymphocytes in vitro and establish lymphoblastoid cell lines (LCLs) [2]. EBV-transformed lymphoblasts express 6 nuclear proteins (Epstein-Barr nuclear antigen [EBNA] 1, 2, 3A, 3B, 3C, and LP) and 3 membrane proteins (latent membrane protein [LMP] 1, 2A, and 2B), and this pattern of EBV gene expression is termed latency III. In contrast, Burkitt lymphoma cells express only EBNA1 consistently (latency I), whereas Hodgkin lymphoma and nasopharyngeal carcinoma cells express EBNA1, LMP1, and LMP2 (latency II). In vivo, EBV-transformed cells are effectively removed by virus-specific cytotoxic T cells, and EBV infection in immunocompetent humans is usually subclinical, except for IM caused by primary infection during adolescence or adulthood. However, in immunocompromised hosts, such as patients with AIDS and transplant recipients, EBV-infected B lymphoblasts can proliferate and cause lymphoproliferative disorder.

Received 28 December 2007; accepted 19 March 2008; electronically published 15 July 2008.

Potential conflicts of interest: none reported.

Financial support: Ministry of Health, Labour, and Welfare of Japan (grants H18-Shinko-013 and H19-AIDS-003).

[a] M.Y. and K.-I.I. contributed equally to this study.

Reprints or correspondence: Dr. Shigeyoshi Fujiwara, Dept. of Infectious Diseases, National Research Institute for Child Health and Development, 2-10-1 Okura, Setagaya-ku, Tokyo 157-8535, Japan (shige@nch.go.jp); or, Dr. Norio Shimizu, Dept. of Virology, Div. of Medical Science, Medical Research Institute, Tokyo Medical and Dental University, 1-5-45 Yushima, Bunkyo-ku, Tokyo 113-8519, Japan (nshivir@tmd.ac.jp); or, Dr. Naoki Yamamoto, AIDS Research Center, National Institute of Infectious Diseases, 1-23-1 Toyama, Shinjuku-ku, Tokyo 162-8640, Japan (nyama@nih.go.jp).

The Journal of Infectious Diseases 2008; 198:673–82

0022-1899/2008/19805-0008$15.00

DOI: 10.1086/590502

EBV infects only humans in nature and limited animal species under experimental conditions. It can infect cotton-top tamarins and induce lymphomas, which have been used as a model of EBV-associated lymphomas [3, 4]. Nonhuman primates possess their own lymphocryptoviruses related to EBV, and research on the use of these virus-host systems as models of EBV infection is currently in progress [5, 6]. Small-animal models of EBV have also been developed, which are particularly useful when a large number of animals are necessary. *Scid* mice that receive intraperitoneal transplants of EBV-transformed LCLs or peripheral blood mononuclear cells (PBMCs) isolated from EBV-infected persons develop lymphomas, which have been used as a model of human lymphoproliferative disorder [7–9]. Recently, NOD/*scid* mice transplanted with human hematopoietic stem cells (HSCs) and reconstituted mainly with B lymphocytes were infected with EBV, and the development of lymphoproliferative disorder was described [10]. The immune response to EBV was not studied in these *scid* or NOD/*scid* mouse models. Very recently, a functional human immune system could be reconstituted in highly immunodeficient mouse strains, and these so-called humanized mice were shown able to mount an EBV-specific T cell response [11, 12]. These studies were, however, performed mainly using immunological standpoints and did not provide detailed virological data.

NOD/Shi-*scid*/IL-2Rγ^{null} (referred to here as NOG) is a highly immunodeficient mouse strain that was developed very recently and that, after transplantation with cord blood HSCs, is able to reconstitute most major components of the hematolymphoid system, including T cells, B cells, NK cells, macrophages, and dendritic cells [13–15]. Human T cells that develop in NOG mice are functional in that they can be activated to display cytotoxic activity [15, 16]. These properties made NOG mice an excellent model of human virus infections targeting the immune system, such as those with human T-lymphotropic virus–1 and HIV-1 [17–20]. Here, we provide evidence that humanized NOG mice can reproduce various key aspects of human EBV infection and propose that they may be a valuable tool for studies of EBV infection.

Table 1. Primers for reverse-transcription polymerase chain reaction to detect Epstein-Barr virus (EBV) transcripts.

Transcript, primer	Sequence (5'→3')
EBNA1	
5'	gatgagcgtttgggagagctgattctgca
3'	tcctcgtccatggttatcac
EBNA2	
5'	agaggaggtggtaagcggttc
3'	tgacgggtttccaagactatcc
LMP1	
5'	ctctccttctcctcctcttg
3'	caggagggtgatcatcagta
LMP2A	
5'	atgactcatctcaacacata
3'	catgttaggcaaattgcaaa
LMP2B	
5'	cagtgtaatctgcacaaaga
3'	catgttaggcaaattgcaaa
EBER1	
5'	agcacctacgctgccctaga
3'	aaaacatgcggaccaccagc
BZLF1 (first)	
5'	attgcaccttgccgccaccttg
3'	cgcattttctggaagccacccga
BZLF1 (second)	
5'	gaccaagctaccagagtctat
3'	cagaatcgcattcctccagcga
BMRF1	
5'	ctagccgtcctgtccaagtgc
3'	agccaaacagctccttgccca
BLLF1	
5'	gtcagtacaccatccagagcc
3'	ttggtagacagccttcgtatg
GAPDH	
5'	gcctcctgcaccaccaactg
3'	cgacgcctgcttcaccaccctct

NOTE. EBNA, Epstein-Barr nuclear antigen; EBER, EBV-encoded small RNA; LMP, latent membrane protein.

METHODS

Preparation of humanized mice. NOG mice were obtained from the Central Institute for Experimental Animals (Kawasaki, Japan). Protocols for experiments with NOG mice were approved by the Institutional Animal Care and Use Committee of the National Institute of Infectious Diseases (NIID). Cord blood was supplied by the Tokyo Cord Blood Bank after obtaining informed consent. The use of human materials in this research was approved by the institutional review boards of the National Research Institute for Child Health and Development, the NIID, the Tokyo Medical and Dental University, and the Tokyo Cord Blood Bank. The isolation of human $CD34^+$ HSCs from cord blood by means of the MACS Direct CD34 Progenitor Cell Isolation Kit (Miltenyi Biotec), their intravenous injection (1×10^4 to 1.2×10^5 cells/mouse) into 6–10-week-old female NOG mice, and the characterization of the reconstitution of the human hematoimmune system were done as described elsewhere [18, 20]. NOG mice in which the human hematoimmune system was reconstituted are referred here as humanized NOG (hNOG) mice.

Experimental EBV infection, quantification of viral DNA, and detection of viral mRNAs. Virus production by EBV-infected Akata cells was stimulated by brief treatment with anti-IgG antibody (Dako), and culture fluid was used as inoculum after filtration through a 0.45-μm membrane filter [21]. For virus titration, cord blood lymphocytes were plated at the density

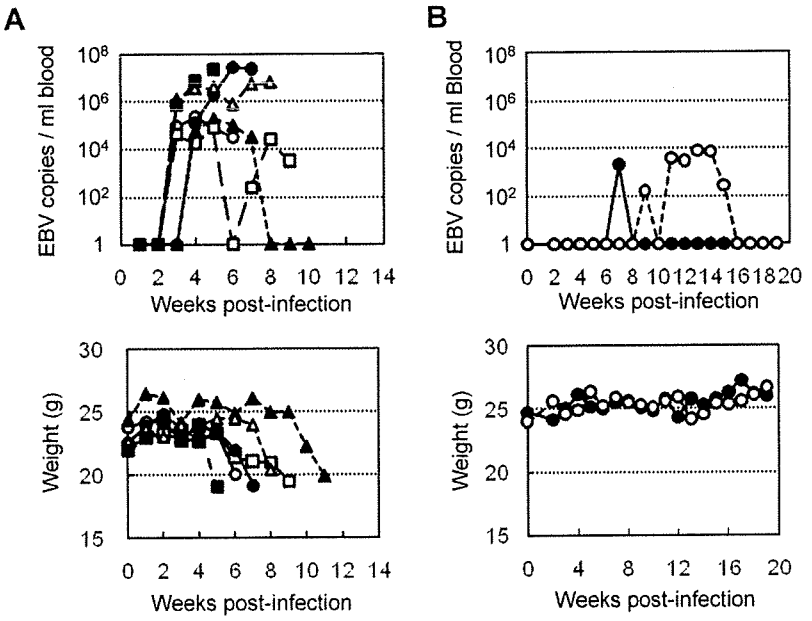

Figure 1. Peripheral blood Epstein-Barr virus (EBV) DNA load and body weight in humanized NOG (hNOG) mice infected with EBV. *A*, Infection at a high dose of virus. Six mice were inoculated intravenously with 1×10^3 TD_{50} of EBV. Peripheral blood EBV DNA load *(upper panels)* and body weight *(lower panels)* were then determined weekly. Each symbol in the graphs represents an individual mouse. Interruption of records indicates the death or killing of a mouse. *B*, Infection at lower doses. Peripheral blood EBV DNA load *(upper panel)* and body weight *(lower panel)* of 2 mice inoculated with low doses of EBV (*black circle*, 1×10^{-1} TD_{50}; *white circle*, 1×10^1 TD_{50}) are shown.

of 2×10^5 cells per well in 6-well plates and then inoculated with serial 10-fold dilutions of virus preparation. The number of wells with proliferating lymphocytes was counted 6 weeks after infection, and the titer of the virus in 50% transforming dose (TD_{50}) was determined by the Reed-Muench method [22]. EBV was inoculated intravenously through the tail vein. EBV DNA was quantified by a real-time quantitative polymerase chain reaction (PCR) assay based on the TaqMan system (Applied Biosystems), as described elsewhere [23]. Analysis of EBV gene expression by reverse-transcription PCR (RT-PCR) was done as described elsewhere, using the primers listed in table 1 [24].

Histopathology, in situ hybridization (ISH), and immunohistochemistry. Tissue samples were fixed in 10% buffered formalin, embedded in paraffin, and stained with hematoxylin-eosin. For phenotypic analysis of proliferating lymphocytes, immunostaining for CD3 (Nichirei), CD4 (Novocastra), CD8 (Nichirei), CD45RO, CD20, CD79a, CD30, Mum1 (Dako), CD23, CD10, CD56 (Novocastra), granzyme B (Dako), and T cell intracellular antigen 1 (Beckman Coulter) was performed on paraffin sections. EBV was detected by immunostaining for LMP1 and EBNA2 (Dako) and by ISH with EBV-encoded small RNA (EBER) probe. Immunohistochemistry and ISH were performed on an automated stainer (Benchmark XT; Ventana Medical Systems), in accordance with the manufacturer's recommendations. To determine the cell lineage of EBV-infected cells, paraffin sections were applied to double staining with EBER ISH and immunohistochemistry.

Detection of EBV-specific T cell response. Enzyme-linked immunospot (ELISPOT) assay was performed with the Immunocyto IFN-γ ELISPOT Kit (MBL), in accordance with the instructions supplied by the manufacturer. Briefly, $CD8^+$ T cells were isolated from PBMCs from EBV-infected hNOG mice with the IMag anti-human CD8 Particles–DM (BD Biosciences). Mixture of these $CD8^+$ T cells and an autologous LCL were incubated with interleukin (IL)–2 in microplates coated with antibody to interferon (IFN)–γ for 17 h. Captured IFN-γ was detected by use of biotinated antibody to IFN-γ and alkaline phosphatase–conjugated streptavidin and was visualized by reaction with the BCIP/NBT chromogen substrate. The unpaired Student's *t* test was used for statistical analysis. IFN-γ secretion in response to EBV was also examined by flow cytometry, as described elsewhere [25]. Briefly, aliquots of murine splenocytes and an LCL were mixed in 6-well plates in the presence of brefeldin A (10 μg/mL) and incubated at 37°C in 5% CO_2 for 17 h. After incubation, the cell suspensions were stained with phycoerythrin-conjugated anti-human CD69, phycoerythrin–Texas red–conjugated anti-human CD45, and phycoerythrin–cyanin 5–conjugated anti-human CD8 for 30 min at 4°C and were fixed with 2% paraformaldehyde. Cells were then permeabilized and stained with BD Perm/Wash buffer (BD Biosciences) containing fluorescein isothiocyanate–conjugated anti-human IFN-γ for 30 min at 4°C. Stained cells were analyzed using an EpicsXL flow cytometer (Beckman Coulter).

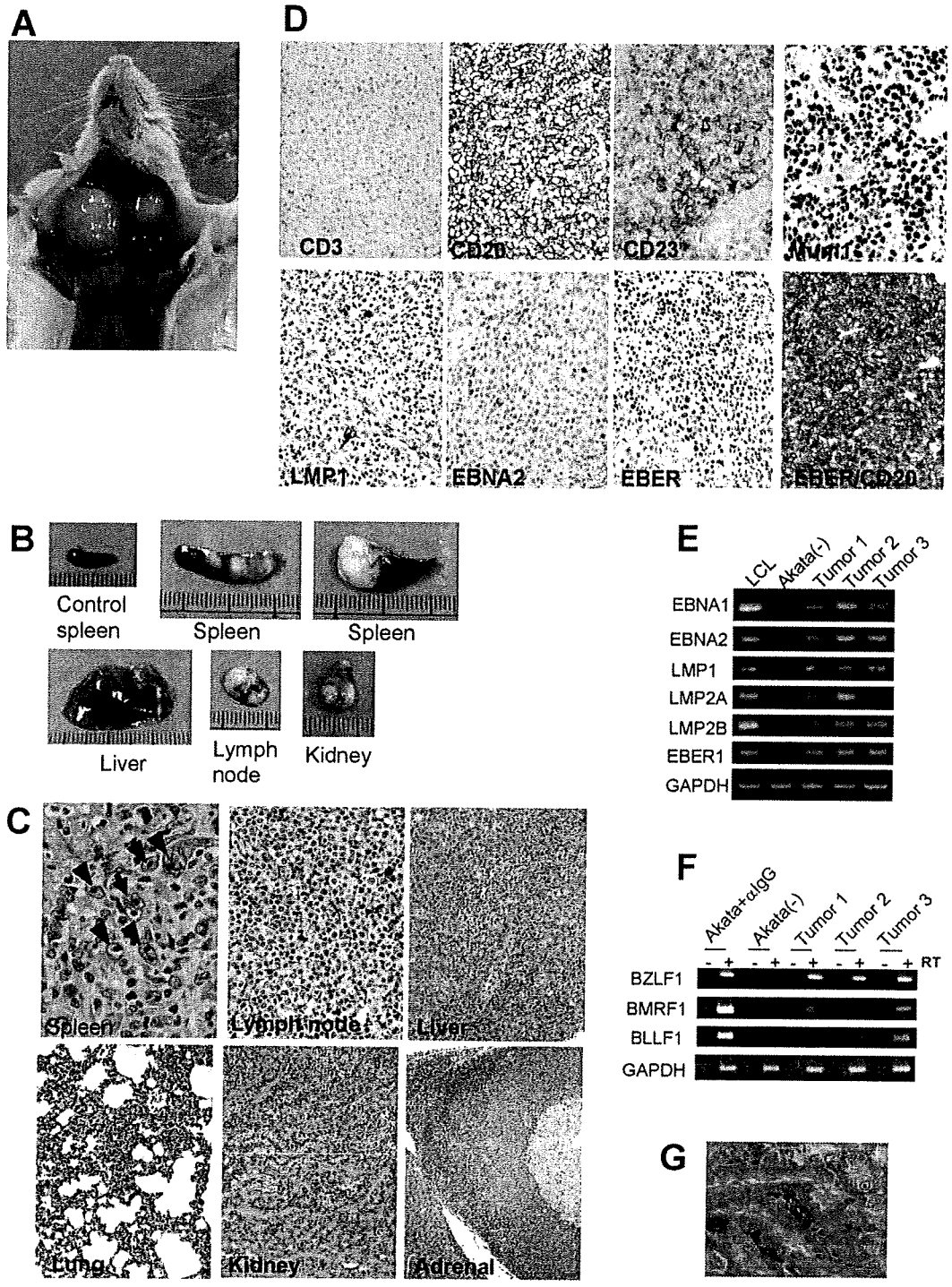

Figure 2. Pathological and virological analyses of Epstein-Barr virus (EBV)–infected humanized NOG (hNOG) mice. *A,* Photograph of an EBV-infected mouse showing tumors in the cervical area. *B,* Photographs of spleens, liver, lymph node, and kidney from EBV-infected mice with lymphoproliferative disorder. The upper left panel shows the spleen from an uninfected mouse. *C,* Photomicrographs of hematoxylin-eosin–stained tissues from mice with lymphoproliferative disorder. The arrow indicates a Reed-Sternberg–like cell, and the arrowheads indicate Hodgkin-like cells. Original magnifications, ×1000 for spleen, ×400 for lymph node, and ×200 for liver, lung, kidney, and adrenal gland. *D,* Immunohistochemical staining for lymphocyte surface markers (CD3, CD20, CD23, and Mum1) and EBV-encoded proteins (latent membrane protein [LMP] 1 and Epstein-Barr nuclear antigen [EBNA] 2), as well as in situ hybridization for EBV-encoded small RNA (EBER), in a lymph node from a mouse with lymphoproliferative disorder. The bottom right panel represents double staining for EBER and CD20. Original magnifications, ×200 for all except EBER/CD20, which is ×400. *E* and *F,* Reverse-transcription polymerase chain reaction detection of latent-cycle *(E)* and lytic-cycle *(F)* EBV gene expression in tumors from EBV-infected hNOG mice. Spleen tumors from 3 different mice were examined for the expression of EBNA1, EBNA2, LMP1, LMP2A, LMP2B, EBER1, BZLF1, BMRF1, and BLLF1. RNA samples from a lymphoblastoid cell line (LCL) *(E)* and anti-IgG–treated Akata cells *(F)* were used as positive controls, and an RNA sample from EBV-negative Akata cells (*E* and *F*) was used as a negative control. Assays were done with (+) or without (−) reverse transcriptase (RT) in panel F. Expression of GAPDH was examined as a reference. *G,* Double staining of EBER and CD20 in the liver of an hNOG mouse that was persistently infected with EBV without developing lymphoproliferative disorder. EBER is stained navy in the nucleus, and CD20 is stained brown in the membrane. Original magnification, ×1000.

Table 2. Quantification of Epstein-Barr virus (EBV) DNA in persistently infected humanized NOG mice.

Organ	Mouse	
	N35-1[a]	N35-3[b]
Bone marrow	ND	4.1×10^4
Spleen	6.2×10^2	5.7×10^3
Liver	ND	2.7×10^4
Lymph node (neck)	1.6×10^3	6.9×10^3
Lymph node (axilla)	ND	2.6×10^2
Lymph node (mesentery)	ND	4.1×10^2
Lungs	2.7×10^3	1.0×10^4
Kidneys	1.2×10^3	4.8×10^4
Adrenal gland	4.4×10^1	8.0×10^5

NOTE. Data are the amounts of EBV DNA measured 22 weeks after infection, in copies per microgram of DNA. ND, not detectable.

[a] Infected at 1×10^{-1} TD_{50}.

[b] Infected at 1×10^1 TD_{50}.

Detection of antibodies specific to EBV. IgM antibody to the EBV BFRF3 protein was detected by immunoblotting essentially as described elsewhere [24], except that horseradish peroxidase–conjugated antibody specific to human IgM (Beckman Coulter) was used as secondary antibody. To prepare the glutathione *s*-transferase (GST)–BFRF3 fusion protein, a DNA fragment spanning the entire coding region of BFRF3 was amplified by PCR (sense primer, 5'-GGCTCGAATTCATGGCACGCCG-GCTGCCC-3'; antisense primer, 5'-GGCTCGGATCCATAC-ACCATGTTTCGTGCCC-3') and inserted to the GST fusion vector pSGENT2, to yield the plasmid pSGENT2-BFRF3. *Escherichia coli* cells harboring pSGENT2-BFRF3 were stimulated with isopropyl β-D-1-thiogalactopyranoside to induce the expression of GST-BFRF3, which was subsequently purified by use of the Bulk GST Purification Module (GE Healthcare).

RESULTS

EBV infection in hNOG mice. Transplantation of human $CD34^+$ HSCs in NOG mice and reconstitution of the human hematoimmune system were done as described elsewhere [18, 20]. In the initial attempts at infection, 1×10^3 TD_{50} of the Akata strain of EBV was inoculated into 6 hNOG mice, and EBV DNA was demonstrated in the peripheral blood of all of them (figure 1*A*). EBV DNA was first evident at 3–4 weeks after inoculation and reached peak levels of $\sim 1 \times 10^6$ EBV DNA copies/μg of DNA. All 6 mice became seriously ill between 5 and 10 weeks after inoculation, with signs of weight loss (figure 1*A*), general inactivity, and piloerection. In contrast, EBV DNA was not detected in the peripheral blood, bone marrow, thymus, spleen, lymph nodes, liver, kidneys, and lungs of 3 control NOG mice that were not transplanted with HSCs but were inoculated with the virus (data not shown). Similarly, no signs of EBV infection were observed in 3 control hNOG mice that were not inoculated with the virus (data not shown). In total, 43 NOG mice that had been humanized with HSCs from 9 different cord blood samples were inoculated with 1×10^3 TD_{50} of EBV, and in 38 of them the results were similar to those observed in the initial 6 mice, with high blood EBV load and severe deterioration in their general condition. Ten of them died and could not be examined further. The remaining 28 mice were killed, and signs of lymphoproliferative disorder were found at autopsy (see the below). These results demonstrate that hNOG mice can be infected with EBV, with a mostly fatal outcome at this virus dose.

EBV-induced lymphoproliferative disorder in hNOG mice. Autopsy of killed mice showed signs of lymphoproliferative disorder typically represented by an overt tumor in the spleen (figure 2*B*). In ~70% (20/28) of the mice autopsied, macroscopical signs of disseminated disease were found in the liver, lymph nodes, or kidneys (figure 2*A* and 2*B*). Seventeen mice were examined pathologically, and 15 of them showed typical histology of diffuse large B cell lymphoma, with remarkable similarity to the human lymphoproliferative disorder in the immunocompromised hosts (figure 2*C*). The tissues contained occasional immunoblasts, Reed-Sternberg–like cells, and Hodgkin-like cells (figure 2*C*). Marked infiltration of large transformed lymphoid cells was also demonstrated in liver, lymph nodes, kidneys, adrenal glands, and lungs (figure 2*C*). Real-time PCR detected high levels ($\sim 1 \times 10^5$ to $\sim 1 \times 10^6$ EBV DNA copies/μg of DNA) of EBV DNA in these organs, and the large transformed lymphoid cells were universally EBV positive by EBER ISH (figure 2*D*). Immunohistochemical analysis showed that the large transformed lymphoid cells were of the activated B cell phenotype, being reactive for CD20 and CD23 and not reactive for CD3 and CD10 (figure 2*D* and data not shown). They were also positive for Mum-1, a late- and postgerminal center cell marker. The EBER-positive cells were CD20-positive B cells (figure 2*D*), and no EBER-positive T cells were identified. Immunostaining revealed that most proliferating cells expressed EBNA2, whereas LMP1 was expressed in only a fraction of them (figure 2*D*). RT-PCR analysis of typical spleen tumors obtained from 3 different mice showed the expression of EBNA1, EBNA2, LMP1, LMP2A, LMP2B; and EBER, consistent with the latency III program of EBV gene expression (figure 2*E*). In addition, transcripts from lytic-cycle EBV genes, including BZLF1 (immediate-early), BMRF1 (early), and BLLF1 (late, encoding gp350/220), were identified (figure 2*F*).

Virus dose–dependent outcome of EBV infection in hNOG mice. To examine the influence of virus dose on the outcome of EBV infection, we inoculated serial dilutions of EBV preparation into 2 lots of hNOG mice, each consisting of 5 mice that had been humanized with the same HSC preparation. Consistent with the results described above, the 4 mice (2 from each lot) that received the higher doses (1×10^3 and 1×10^2 TD_{50}) of the

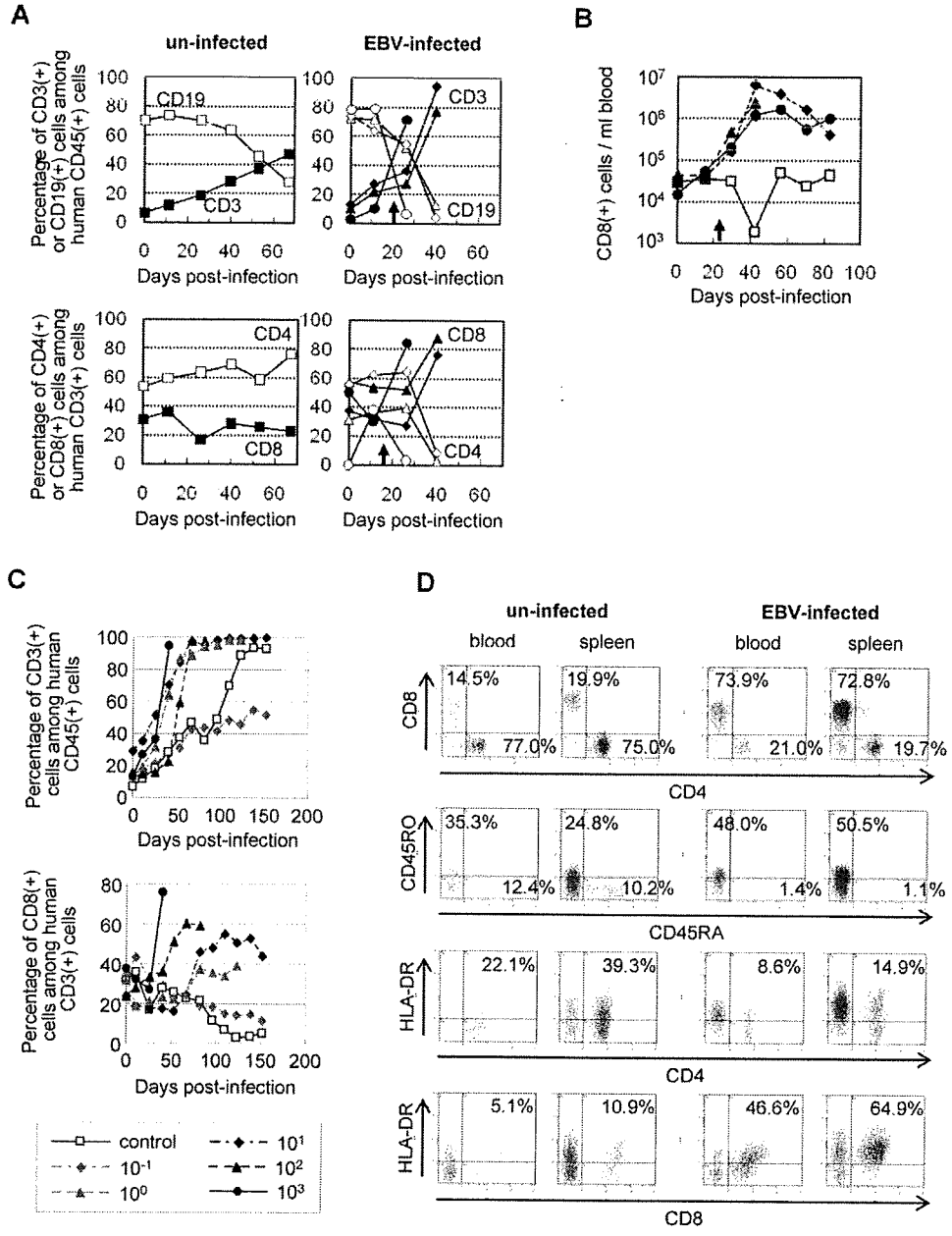

Figure 3. Surface marker expression by peripheral blood T cells in Epstein-Barr virus (EBV)–infected humanized NOG (hNOG) mice. *A,* Changes in the percentages of $CD3^+$ T cells and $CD19^+$ B cells among human $CD45^+$ leukocytes *(upper panels)* and in the percentages of $CD8^+$ cells and $CD4^+$ cells among $CD3^+$ cells *(lower panels)* after infection with EBV. Results obtained from 3 EBV-infected mice and an uninfected mice are shown. White symbols indicate the percentage of $CD19^+$ cells *(upper panels)* or $CD4^+$ cells *(lower panels);* black symbols indicate the percentage of $CD3^+$ cells *(upper panels)* or $CD8^+$ cells *(lower panels).* A vertical arrow in the graph area shows the time point at which EBV DNA was first detected in peripheral blood. *B,* Changes in the no. of $CD8^+$ T cells in the peripheral blood of EBV-infected hNOG mice. White symbols indicate uninfected mice, and black symbols indicate infected mice. Note that cell no. is plotted in a logarithmic scale. *C,* Viral dose–dependent T cell responses in hNOG mice inoculated with serially diluted EBV. Ten-fold serial dilutions of an EBV sample starting from 1×10^3 TD_{50} per inoculate were injected intravenously into NOG mice that had undergone transplantation with the same lot of human hematopoietic stem cells (HSCs). Changes in the percentages of $CD3^+$ T cells among human $CD45^+$ leukocytes *(upper panel)* and in the percentages of $CD8^+$ cells among $CD3^+$ cells *(lower panel)* after inoculation with EBV are shown. The viral dose for each mouse is shown in the key. *D,* Comparison of surface marker expression between EBV-infected mice and control mice. Two mice that underwent transplantation with the same lot of human HSCs were either inoculated with EBV or left uninfected; 10 weeks after inoculation, mononuclear cells obtained from peripheral blood or spleen were gated for the expression of human CD3 and then examined for the expression of CD8 and CD4 *(top panels),* CD45RO and CD45RA *(second from top),* HLA-DR and CD4 *(second from bottom),* and HLA-DR and CD8 *(bottom).*

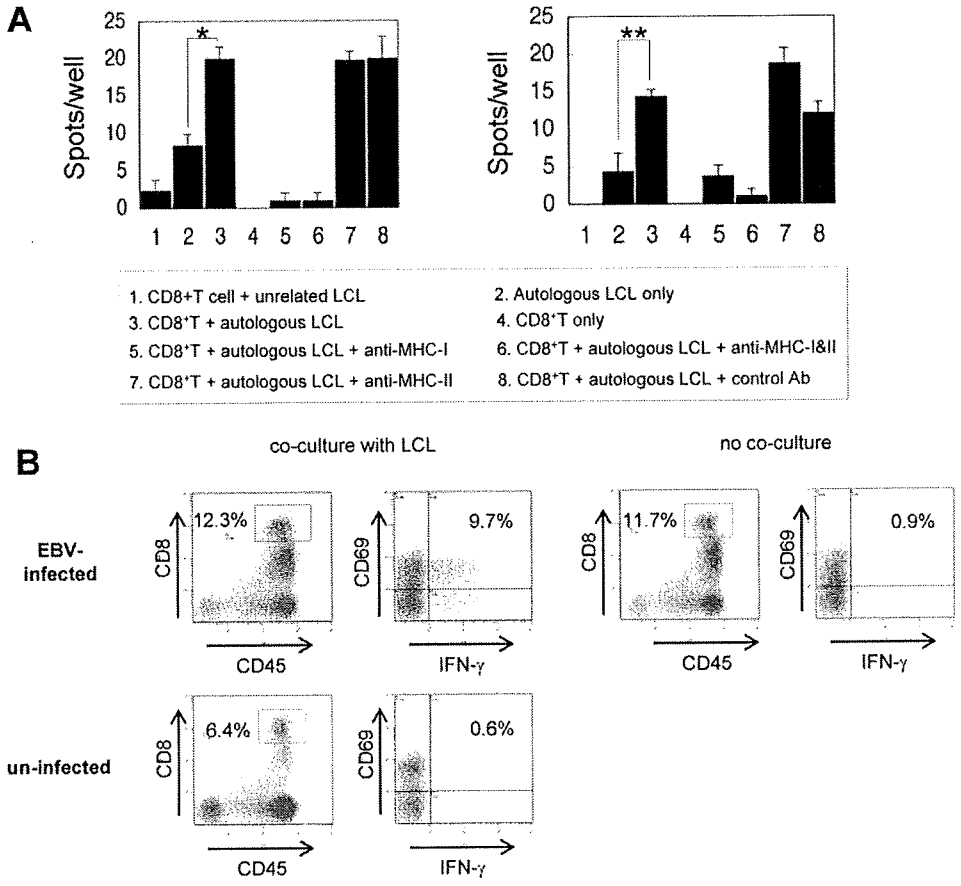

Figure 4. Epstein-Barr virus (EBV)–specific T cell response in humanized NOG (hNOG) mice. *A,* Enzyme-linked immunospot assay for the detection of human T cells producing interferon (IFN)–γ after stimulation with an EBV-positive lymphoblastoid cell line (LCL). $CD8^+$ cells isolated from EBV-infected hNOG mice were cocultured with an autologous LCL, and IFN-γ–secreting cells were counted (3, 5, 6, 7, and 8). To analyze restriction by major histocompatibility complex (MHC), antibody to HLA class I (anti–human HLA-ABC clone W6/32; eBioscience) (5), antibodies to both HLA class I and class II (6), antibody to HLA class II (anti–human HLA-DP,DQ,DR clone CR3/43; Dako) (7), or isotype-matched control antibody (8) were added to the culture. Control experiments included coculture of $CD8^+$ cells with an MHC-mismatched LCL (1), culture of the autologous LCL only (2), and culture of $CD8^+$ cells only (4). Results from 2 infected mice are shown. Five hundred $CD8^+$ cells per well were cultured in the experiment shown on the left, and 250 $CD8^+$ cells per well were cultured in that shown on the right. Spots were counted in triplicate in each of the 8 experimental groups, and the bars represent mean values and SEs. The unpaired Student's *t* test was used for statistical analysis. $^*P < .01$ and $^{**}P < .02$. *B,* Detection of human $CD8^+$ cells that produce IFN-γ in response to stimulation with an EBV-positive LCL by flow cytometry. $CD8^+$ cells were isolated from the spleen of an EBV-infected mouse and cocultured with the autologous LCL. Intracellular IFN-γ was stained and analyzed as described in Methods.

virus died of lymphoproliferative disorder ~5–10 weeks after inoculation. The remaining mice in both of the lots that received lower doses (1×10^1, 1×10^0, and 1×10^{-1} TD_{50}) survived acute infection and appeared normal throughout the observation period of 22 weeks. Although EBV DNA was detected at variable levels in their peripheral blood several weeks after inoculation, it returned to undetectable levels thereafter (figure 1*B*), suggesting that a certain protection mechanism worked to control EBV infection. Importantly, EBV DNA could be still detected in various organs, including spleen, liver, lungs, kidneys, and adrenal glands, at the end of the observation period (22 weeks), indicating that EBV persisted in these mice (table 2). Double staining for EBER and CD20 showed that EBV persisted in B cells (figure 2*G*). Macroscopical examination by autopsy at the end of the observation period did not reveal abnormality in these mice, except for moderate splenomegaly found in a mouse that received 1×10^1 TD_{50}. These results indicate that the outcome of EBV infection in hNOG mice varies with the virus dose; high doses of virus tend to cause fatal lymphoproliferative disorder, whereas lower doses induce apparently asymptomatic persistent infection.

EBV-specific T cell response in hNOG mice. Flow cytometry analysis demonstrated a dramatic increase in the percentage of $CD3^+$ T cells among the human $CD45^+$ leukocytes after infection with EBV. This increase in T cells was accompanied by an increase in the percentage of $CD8^+$ cells among human $CD3^+$ T cells. These changes were seen in virtually all infected mice, and the results from 3 mice are shown in figure 3*A*. The slow increase in the percentage of $CD3^+$ cells in the uninfected mouse represents the process of humanization (i.e., the development of hu-

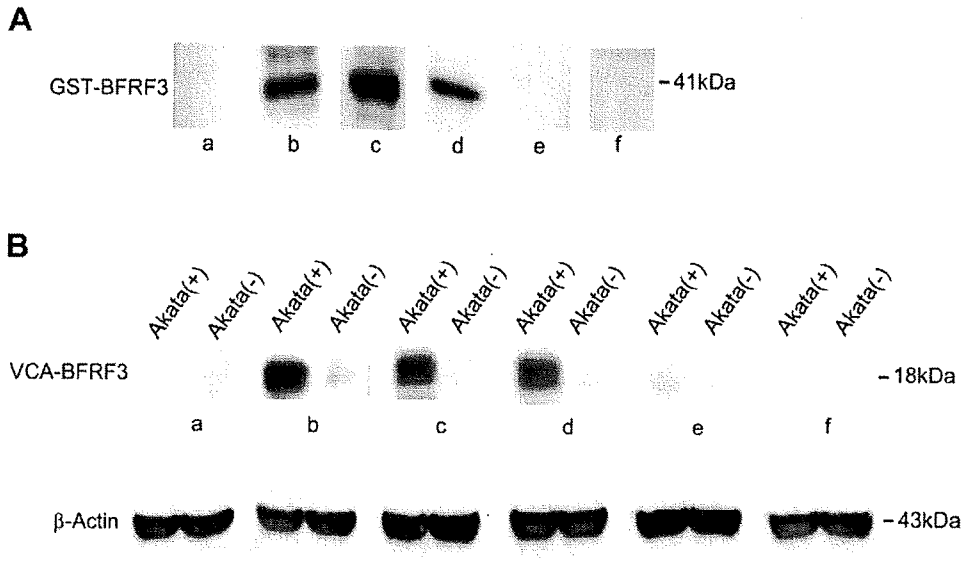

Figure 5. Demonstration of IgM antibody to the Epstein-Barr virus (EBV) BFRF3 protein in the serum of humanized NOG (hNOG) mice. *A*, Immunoblot with the glutathione *s*-transferase (GST)–BFRF3 fusion protein. Purified GST-BFRF3 fusion protein was examined with serum from an EBV-uninfected person *(a)*, an EBV-infected person *(b)*, EBV-infected hNOG mice (*c* and *d*), and an uninfected hNOG mice (*e* and *f*). *B*, Immunoblot with the lysate of EBV-producing Akata cells. Lysate of anti-IgG–treated Akata cells, labeled Akata(+), and of EBV-negative Akata cells, labeled Akata(−), was examined using serum from an EBV-uninfected person *(a)*, an EBV-infected person *(b)*, EBV-infected hNOG mice (*c* and *d*), and uninfected hNOG mice (*e* and *f*).

man T cells). This increase in $CD8^+$ cells were even more conspicuous when their definite number was counted (figure 3*B*). When hNOG mice were inoculated with serially diluted virus samples, a striking dose response was evident; mice inoculated with higher doses exhibited a more profound increase in $CD8^+$ cells at earlier time points (figure 3*C*). Further flow cytometry analyses showed that $CD45RO^+$ memory T cells, compared with $CD45RA^+$ T cells, increased in infected hNOG mice (figure 3*D*). Expression of a T cell activation marker, HLA-DR, was observed mainly in $CD8^+$ cells rather than in $CD4^+$ cells (figure 3*D*).

To demonstrate that these $CD8^+$ T cells were directed against EBV-infected cells, we examined IFN-γ secretion after stimulation with EBV-transformed cells. For this purpose, we first established an LCL using B cells isolated from the same cord blood that was used to isolate HSCs for transplantation. $CD8^+$ T cells, isolated from the peripheral blood of EBV-infected hNOG mice, were incubated with this autologous LCL, and cells secreting IFN-γ were detected by ELISPOT assay. For all 3 EBV-infected hNOG mice (which had been infected at 1×10^3 TD_{50}) thus examined, a significant number of spots were recognized in the wells in which $CD8^+$ T cells were mixed with the autologous LCL, whereas those cells incubated with unrelated LCL had many fewer spots (data from 2 mice are shown in figure 4*A*). $CD8^+$ T cells isolated from uninfected hNOG mice did not give a significant number of spots (data not shown). Release of IFN-γ was blocked by antibody specific to human major histocompatibility complex (MHC) class I but not by that specific to human MHC class II (figure 4*A*). These results clearly show that a T cell response restricted by human MHC class I was mounted against EBV-infected cells. In addition, in 5 of the 6 EBV-infected hNOG mice examined (infected at 1×10^3 TD_{50}), flow cytometry also demonstrated production of IFN-γ by $CD8^+$ T cells isolated from the spleen and stimulated with an autologous LCL (figure 4*B*).

EBV-specific antibody response in hNOG mice. Serum samples from 30 EBV-infected hNOG mice were examined by Western blotting for IgM antibodies reactive with a bacterially expressed GST-BFRF3 fusion protein. The BFRF3 protein is a major component of the virus capsid antigen of EBV [26]. The results are shown in figure 5*A* and indicated that four serum samples (from mice infected at 1×10^1 or 1×10^3 TD_{50}) contained IgM antibody reactive with it. These serum samples reacted also with the 18-kDa BFRF3-encoded protein in the lysate of Akata cells stimulated with IgG antibody to activate virus production (figure 5*B*). Similar experiments with human IgG–specific secondary antibody did not show a positive reaction with either GST-BFRF or $p18^{BFRF3}$. Six serum samples collected from uninfected hNOG mice reacted with neither the 18-kDa protein nor GST-BFRF3 (figure 5 and data not shown). These results indicate that hNOG mice have the ability to mount an IgM response to EBV.

DISCUSSION

The lymphoproliferative disease induced in hNOG mice is remarkably similar to the human lymphoproliferative disorder seen in immunocompromised hosts [27] with respect to histology, surface phenotype, and the type of EBV gene expression

(latency III). Reproduction of latency III in the present study makes for an interesting contrast with the previous model using NOD/*scid* mice, which exhibited the latency II pattern [10].

EBV infection in lower doses resulted in a transient increase in EBV DNA load in the peripheral blood, followed by apparently asymptomatic infection that persisted for at least 22 weeks. This type of asymptomatic EBV infection has not been described in nonprimate models of EBV infection and may be regarded as a model of human EBV latency. To compare this condition in NOG mice with EBV latency in humans precisely, we need to further investigate the nature of host cells (i.e., whether they are memory B cells), the pattern of EBV gene expression in them, and the involvement of anti-EBV immune responses in its maintenance.

In hNOG mice, human T cells develop in thymus tissue, in which epithelial cells are of murine origin [16]. It is therefore interesting that they could mount a T cell response restricted by human MHC class I. Although this suggests that positive selection of human T cells occurred in hNOG mice, the mechanism of T cell education remains unclear. Alloantigen-specific and human MHC class I–restricted T cell cytotoxicity has been reported in hNOG mice [15, 16]. An EBV-induced T cell response was evident in mice that received high doses of virus and developed lymphoproliferative disorder, suggesting that the T cell response in hNOG mice was not sufficient to control EBV-induced lymphoproliferation when they were infected at high doses. That only a minor fraction of $CD8^+$ T cells appeared to be EBV specific, as evidenced by ELISPOT assay and flow cytometry, may explain this result, at least partially. A humoral immune response to EBV has not been documented in previous mouse models of EBV infection, and therefore the NOG mouse may provide a valuable tool to analyze the mechanism and the protective roles of antibody response in EBV infection. We have to date clearly identified only IgM antibody to the 18-kDa component of virus capsid antigen in a minor fraction (4/30) of infected mice. We are currently attempting to improve sensitivity and to see whether hNOG mice can mount a more efficient and divergent antibody response to the virus, possibly including the production of IgG antibodies. Because both the T cell–mediated and the humoral immune response are elicited in hNOG mice, they may be useful in the evaluation of candidate EBV vaccines.

Very recently, humanized mice based on other immunodeficient mouse strains were prepared, and EBV was used as a typical pathogen to analyze their immune functions. Traggiai et al. [12] infected humanized $Rag2^{-/-}IL\text{-}2R\gamma^{-/-}$ mice with EBV and documented an in vitro proliferative response by $CD8^+$ T cells to an autologous LCL. Melkus et al. [11], on the other hand, humanized NOD/*scid* mice by transplanting human fetal liver, thymus, and HSCs and succeeded in inducing an EBV-specific T cell immune response as well as an innate immune response to toxic shock syndrome toxin 1. These 2 studies were performed mainly using immunological standpoints and did not provide detailed data from virological investigations. An advantage of the NOG mouse model described here is that it does not require a fine surgical procedure using human fetal tissue; therefore, NOG mice can be easily provided in large quantities.

In immunocompromised humans, failure of immunosurveillance may lead to the development of lymphoproliferative disorder. We expect that the NOG mouse model can be used to analyze the exact relationship between immunodeficiency and the development of lymphoproliferative disorder. Immune responses in the hNOG mouse can be modulated by immunosuppressive drugs (such as cyclosporine A) or HIV, and the development of lymphoproliferative disorder can be analyzed with special reference to the nature and level of immunodeficiency. This kind of study, which has not been possible with conventional *scid* mice, may reveal an exact condition in which lymphoproliferative disorder develops and may thereby aid the development of a specified immunosuppressive procedure that evades this condition and precludes the risk of lymphoproliferative disorder.

In summary, the NOG mouse is able to recapitulate various essential elements of human EBV infection and is therefore, to our knowledge, the most comprehensive small-animal model of EBV infection described to date. It should be a valuable tool for the study of the pathogenesis, prevention, and treatment of EBV infection.

Acknowledgments

We thank Satoshi Itakura, Fuyuko Kawano, Eri Yamada, Miki Mizukami, and Ken Watanabe for technical assistance. We thank Shizuko Minegishi for advice on flow cytometry, Atsushi Komano for advise on the enzyme-linked immunospot assay, Ayako Demachi-Okamura and Kiyotaka Kuzushima for advice on detection of Epstein-Barr virus–specific T cells, and Shosuke Imai for helpful discussions. We thank the Tokyo Cord Blood Bank for supplying cord blood.

References

1. Rickinson AB, Kieff E. Epstein-Barr virus. In: Knipe DM, Howley PM, eds. Fields virology. Philadelphia: Lippincott Williams & Wilkins, **2001**: 2575–628.
2. Kieff E, Rickinson AB. Epstein-Barr virus and its replication. In: Knipe DM, Howley PM, eds. Fields virology. 4th ed. Philadelphia: Lippincot Williams & Wilkins, **2001**:2511–74.
3. Young LS, Finerty S, Brooks L, Scullion F, Rickinson AB, Morgan AJ. Epstein-Barr virus gene expression in malignant lymphomas induced by experimental virus infection of cottontop tamarins. J Virol **1989**; 63: 1967–74.
4. Miller G, Shope T, Coope D, et al. Lymphoma in cotton-top marmosets after inoculation with Epstein-Barr virus: tumor incidence, histologic spectrum antibody responses, demonstration of viral DNA, and characterization of viruses. J Exp Med **1977**; 145:948–67.
5. Cho Y, Ramer J, Rivailler P, et al. An Epstein-Barr-related herpesvirus from marmoset lymphomas. Proc Natl Acad Sci USA **2001**; 98:1224–9.
6. Moghaddam A, Rosenzweig M, Lee-Parritz D, Annis B, Johnson RP, Wang F. An animal model for acute and persistent Epstein-Barr virus infection. Science **1997**; 276:2030–3.
7. Mosier DE, Gulizia RJ, Baird SM, Wilson DB. Transfer of a functional human immune system to mice with severe combined immunodeficiency. Nature **1988**; 335:256–9.

8. Okano M, Taguchi Y, Nakamine H, et al. Characterization of Epstein-Barr virus-induced lymphoproliferation derived from human peripheral blood mononuclear cells transferred to severe combined immunodeficient mice. Am J Pathol **1990**; 137:517–22.
9. Rowe M, Young LS, Crocker J, Stokes H, Henderson S, Rickinson AB. Epstein-Barr virus (EBV)-associated lymphoproliferative disease in the SCID mouse model: implications for the pathogenesis of EBV-positive lymphomas in man. J Exp Med **1991**; 173:147–58.
10. Islas-Ohlmayer M, Padgett-Thomas A, Domiati-Saad R, et al. Experimental infection of NOD/SCID mice reconstituted with human CD34+ cells with Epstein-Barr virus. J Virol **2004**; 78:13891–900.
11. Melkus MW, Estes JD, Padgett-Thomas A, et al. Humanized mice mount specific adaptive and innate immune responses to EBV and TSST-1. Nat Med **2006**; 12:1316–22.
12. Traggiai E, Chicha L, Mazzucchelli L, et al. Development of a human adaptive immune system in cord blood cell-transplanted mice. Science **2004**; 304:104–7.
13. Hiramatsu H, Nishikomori R, Heike T, et al. Complete reconstitution of human lymphocytes from cord blood CD34+ cells using the NOD/SCID/γ_c^{null} mice model. Blood **2003**; 102:873–80.
14. Ito M, Hiramatsu H, Kobayashi K, et al. NOD/SCID/γ_c^{null} mouse: an excellent recipient mouse model for engraftment of human cells. Blood **2002**; 100:3175–82.
15. Yahata T, Ando K, Nakamura Y, et al. Functional human T lymphocyte development from cord blood CD34+ cells in nonobese diabetic/Shi-scid, IL-2 receptor gamma null mice. J Immunol **2002**; 169:204–9.
16. Ishikawa F, Yasukawa M, Lyons B, et al. Development of functional human blood and immune systems in NOD/SCID/IL2 receptor γ chain^{null} mice. Blood **2005**; 106:1565–73.
17. Miyazato P, Yasunaga J, Taniguchi Y, Koyanagi Y, Mitsuya H, Matsuoka M. De novo human T-cell leukemia virus type 1 infection of human lymphocytes in NOD-SCID, common gamma-chain knockout mice. J Virol **2006**; 80:10683–91.
18. Watanabe S, Terashima K, Ohta S, et al. Hematopoietic stem cell-engrafted NOD/SCID/IL2Rgamma null mice develop human lymphoid systems and induce long-lasting HIV-1 infection with specific humoral immune responses. Blood **2007**; 109:212–8.
19. Dewan MZ, Terashima K, Taruishi M, et al. Rapid tumor formation of human T-cell leukemia virus type 1-infected cell lines in novel NOD-SCID/gammac^{null} mice: suppression by an inhibitor against NF-kappaB. J Virol **2003**; 77:5286–94.
20. Watanabe S, Ohta S, Yajima M, et al. Humanized NOD/SCID/IL2Rγ^{null} mice transplanted with hematopoietic stem cells under nonmyeloablative conditions show prolonged life spans and allow detailed analysis of human immunodeficiency virus type 1 pathogenesis. J Virol **2007**; 81: 13259–64.
21. Takada K, Ono Y. Synchronous and sequential activation of latently infected Epstein-Barr virus genomes. J Virol **1989**; 63:445–9.
22. Condit RC. Principles of virology. In: Knipe DM, Howley PM, eds. Fields virology. Philadelphia: Lippincott Williams & Wilkins, **2001**:19–51.
23. Kimura H, Morita M, Yabuta Y, et al. Quantitative analysis of Epstein-Barr virus load by using a real-time PCR assay. J Clin Microbiol **1999**; 37:132–6.
24. Nakamura H, Iwakiri D, Ono Y, Fujiwara S. Epstein-Barr-virus-infected human T-cell line with a unique pattern of viral-gene expression. Int J Cancer **1998**; 76:587–94.
25. Kuzushima K, Hoshino Y, Fujii K, et al. Rapid determination of Epstein-Barr virus-specific CD8$^+$ T-cell frequencies by flow cytometry. Blood **1999**; 94:3094–100.
26. van Grunsven WM, Nabbe A, Middeldorp JM. Identification and molecular characterization of two diagnostically relevant marker proteins of the Epstein-Barr virus capsid antigen complex. J Med Virol **1993**; 40: 161–9.
27. Rezk SA, Weiss LM. Epstein-Barr virus-associated lymphoproliferative disorders. Hum Pathol **2007**; 38:1293–304.

ELSEVIER

INSTITUT PASTEUR

Microbes and Infection 10 (2008) 748–756

www.elsevier.com/locate/micinf

Original article

Induction of apoptosis in Epstein-Barr virus-infected B-lymphocytes by the NF-κB inhibitor DHMEQ

Ariko Miyake [a,1], Md. Zahidunnabi Dewan [b,c,1], Takaomi Ishida [a], Mariko Watanabe [d], Mitsuo Honda [c], Tetsutaro Sata [e], Naoki Yamamoto [b,c,**], Kazuo Umezawa [f], Toshiki Watanabe [a,***], Ryouichi Horie [d,*]

[a] *Laboratory of Tumor Cell Biology, Department of Medical Genome Sciences, Graduate School of Frontier Sciences, University of Tokyo, 4-6-1 Shirokanedai, Minato-ku, Tokyo 108-8639, Japan*

[b] *Department of Molecular Virology, Bio-Response, Graduate School, Tokyo Medical and Dental University, 1-5-45 Yushima, Bunkyo-ku, Tokyo 113-8519, Japan*

[c] *AIDS Research Center, National Institute of Infectious Diseases, 1-23-1 Toyama, Shinjuku-ku, Tokyo 162-8640, Japan*

[d] *Department of Hematology, School of Medicine, Kitasato University, 1-15-1 Sagamihara, Kanagawa 228-8555, Japan*

[e] *Department of Pathology, National Institute of Infectious Diseases, 1-23-1 Toyama, Shinjuku-ku, Tokyo 162-8640, Japan*

[f] *Department of Applied Chemistry, Faculty of Science and Technology, Keio University, 3-14-1 Hiyoshi, Kohoku-ku, Yokohama, Kanagawa 223-0061, Japan*

Received 19 January 2008; accepted 9 April 2008
Available online 13 April 2008

Abstract

Epstein–Barr virus (EBV) causes EBV-associated lymphoproliferative diseases in patients with profound immune suppression. Most of these diseases are life-threatening and the prognosis of AIDS-associated lymphomas is extremely unfavorable. Polyclonal expansion of virus infected B-cell predisposes them to transformation. We investigated the possibility of nuclear factor kappa B (NF-κB) inhibition by dehydroxymethylepoxyquinomicin (DHMEQ) for the treatment and prevention of EBV-associated lymphoproliferative diseases. We examined the effect of DHMEQ on apoptosis induction in four EBV-transformed lymphoblastoid cell lines as well as peripheral blood mononuclear cells infected with EBV under immunosuppressed condition. DHMEQ inhibits NF-κB activation in EBV-transformed lymphoblastoid cell lines and induces apoptosis by activation of mitochondrial and membranous pathways. Using an *in vivo* NOD/SCIDγc mouse model, we showed that DHMEQ has a potent inhibitory effect on the growth of lymphoblastoid cells. In addition, DHMEQ selectively purges EBV-infected cells expressing latent membrane protein (LMP) 1 from peripheral blood mononuclear cells and inhibits the outgrowth of lymphoblastoid cells. These results suggest that NF-κB is a molecular target for the treatment and prevention of EBV-associated lymphoproliferative diseases. As a potent NF-κB inhibitor, DHMEQ is a potential compound for applying this strategy in clinical medicine.

Keywords: Epstein–Barr virus infections; NF-κB; DHMEQ

1. Introduction

Epstein–Barr virus (EBV) is a member of the γ-herpesvirus family that infects more than 90% of the world population and initially establishes latency III infection in B lymphocytes [1]. Latency III infection is characterized by the expression of the entire array of EBV latency genes, including EBV nuclear proteins (EBNA1, -2, -3A, -3B, -3C, and -LP), integral latent membrane proteins (LMP1, -2A, and -2B), the BamA

* Corresponding author. Tel.: +81 42 778 8111; fax: +81 42 778 8441.
** Tel.: +81 3 5803 5178; fax: +81 3 5803 0124.
*** Tel.: +81 3 5449 5298; fax: +81 3 5449 5418.
E-mail addresses: yamamoto.mmb@tmd.ac.jp (N. Yamamoto), tnabe@ims.u-tokyo.ac.jp (T. Watanabe), rhorie@med.kitasato-u.ac.jp (R. Horie).
[1] These authors contributed equally to this work.

1286-4579/$ - see front matter © 2008 Elsevier Masson SAS. All rights reserved.
doi:10.1016/j.micinf.2008.04.002

rightward transcripts (BARTs), and small RNAs (EBERs). Immune response mediated by T-lymphocytes eliminates most latency III-infected cells; however, resting memory B lymphocytes provide a reservoir for latent virus. T-lymphocyte immunity to latency III-infected B lymphocytes persists for life and protects reactivation of latent virus from a reservoir [2].

However, in the absence of an effective immune response, reactivation of latent virus from a reservoir occurs and causes EBV-associated lymphoproliferative diseases. EBV-associated lymphoproliferative diseases occur with primary infection after transplantation or reactivation of latent virus as a consequence of immune suppression for organ transplantation and autoimmune diseases or acquired immune deficiency syndrome (AIDS) [3–6]. EBV-associated lymphoproliferative diseases are associated in the majority of cases with latency type III phenotype. The prognosis of EBV-associated lymphoproliferative diseases is variable; however, most of these are life-threatening and the prognosis of AIDS-associated lymphomas is extremely unfavorable, although introduction of highly active anti-retroviral treatment (HAART) decreased the incidence, increased the effectiveness of chemotherapy, and improved survival [5]. EBV infection of B-lymphocytes *in vitro* also results in latency III infection and sustained cell proliferation as lymphoblastoid cell lines (LCLs).

Activation of nuclear factor kappa B (NF-κB) has been connected with resistance against apoptosis and tumorigenesis [7]. Despite the diversity in clinical manifestations of EBV-associated lymphoproliferative diseases, strong and constitutive NF-κB activity is reported to be a common characteristic of this disease entity. LMP1 mimics signaling from tumor necrosis factor (TNF) receptor family members by association with tumor necrosis factor receptor-associated factors (TRAFs) and activates the IKK (IκB kinase)—NF-κB pathway [8].

NF-κB represents five cellular proteins: c-Rel, RelA (p65), RelB, NF-κB1 (p50 and its precursor p105), and NF-κB2 (p52 and its precursor p100). The IκB inhibitory proteins consist of IκBα, IκBβ, IκBε, IκBγ, and Bcl-3. NF-κB forms homo- or heterodimers and exists as an inactive complex with IκB regulatory proteins in the cytoplasm. Various signaling pathways converge into IKK-mediated degradation of IκB proteins and subsequent release of uncomplexed NF-κB, which then migrates into the nucleus and activates the transcription of target genes [9].

Dehydroxymethylepoxyquinomicin (DHMEQ) is a new NF-κB inhibitor that is a 5-dehydroxymethyl derivative of the novel compound epoxyquinomicin C that has a 4-hydroxy-5,6-epoxycyclohexenone structure like panepoxydone. Panepoxydone had been found to inhibit TNF-α-induced activation of NF-κB [10]. We have shown that DHMEQ inhibits NF-κB at the level of nuclear translocation [11].

In this study, to investigate the possibility of NF-κB inhibition by DHMEQ as a strategy for the treatment and prevention of EBV-associated lymphoproliferative diseases, we investigated the effect of DHMEQ on apoptosis induction in four EBV-transformed LCLs as well as peripheral blood mononuclear cells (PBMC) in the early phase of EBV infection, and further examined the molecular mechanism of DHMEQ-induced apoptosis.

2. Materials and methods

2.1. Cells

B95.8 EBV-transformed LCLs were established by infection of lymphocytes from four healthy donors with culture supernatants of the virus producer B95.8 line as described previously [12], and are indicated in the text by the first two letters of the name of each donor. In all experiments to test the effects of DHMEQ treatment, LCLs were maintained in RPMI 1640 medium supplemented with 10% fetal bovine serum (FBS).

2.2. Chemicals

DHMEQ is an NF-κB inhibitor that blocks nuclear translocation of NF-κB [11]. DHMEQ was dissolved with dimethylsulfoxide (DMSO). DHMEQ or DMSO was used for experiments at indicated concentrations. Bisbenzimide H 33342 fluorochrome (Hoechst 33342) was purchased from Calbiochem (Bad Soden, Germany).

2.3. Electrophoretic mobility shift analysis

Electrophoretic mobility shift analysis (EMSA) was carried out according to the methods described previously [13]. For detecting NF-κB binding, a double-stranded oligonucleotide containing the κB site of the promoter for the mouse H-2Kb class I major histocompatibility antigen gene was used as a probe [14]. The nucleotide sequence is 5′-GAT CCG GCT GGG AAT CCC CGC TGG GAA TCC CCA TCT A-3′. For control EMSA, a double-strand oligonucleotide containing Oct-1 consensus sequence (Promega, Madison, WI, USA) was used as a probe. Antibodies used for supershift assays were as follows: NF-κB p50 (C-19) goat polyclonal antibody, rabbit polyclonal antibody for NF-κB p65 (C-20) and RelB (C-19), and mouse monoclonal antibody for c-Rel (B-6) and NF-κB p52 (C-5) (all from Santa Cruz Biotechnology Inc., Santa Cruz, CA). A mouse IgG antibody (Sigma, St. Louis, MO) served as a control.

2.4. Cell viability assay

The effects of DHMEQ on cell viability were assayed by color reaction with a tetrazolium salt, WST-8(4-[3-(2-methoxy-4-nitrophenyl)-2-[4-nitrophenyl]-2*H*-5-tetrazolio]-1,3-benzene disulfonate sodium salt) (Cell Counting Kit-8; Dojindo Laboratories, Kumamoto, Japan). After incubation with DHMEQ or DMSO at the indicated concentrations and time points, cells were treated with Cell Counting Kit-8 according to the manufacturer's recommendations and the results were measured by a microplate reader (Bio-Rad, Richmond, CA) at a test wavelength of 450 nm and reference wavelength of 630 nm.

2.5. Analysis of apoptosis and caspase activities

To quantify apoptosis, cells were labeled with fluorescein isothiocyanate (FITC)-conjugated Annexin V (BD Biosciences, Palo Alto, CA), then subjected to flow cytometric analysis. For analysis of nuclear DNA fragmentation, the terminal deoxynucleotidyl transferase (TdT)-mediated dUTP nick end-labeling (TUNEL) assay was done according to the manufacturer's recommendations (DeadEnd Fluorometric TUNEL Systems; Promega). Cells were analyzed using a FACS Calibur flow cytometer (BD Biociences) and fluorescence microscopy. Activities of caspase-3, -8, and -9 were determined by using green fluorochrome-labeled inhibitors of caspases (FLICA)-3, -8, and -9 (FLICA Apoptosis Detection Kit; Immunochemistry Technologies, Bloomington, MN). Cells from LCLs were treated with 10 μg/ml of DHMEQ (+) or with DMSO alone (−) for 8 h and fixed on slides; active caspases were detected by FLICA-3, -8, and -9. For detection of nuclear DNA, cells were stained with Hoechst 33342 and photographed through a UV filter and an Olympus BX50F microscope (Olympus, Tokyo, Japan).

2.6. In vivo effects of DHMEQ on NOG mice inoculated with LCLs

NOG mice were purchased from the Central Institute for Experimental Animals (Kawasaki, Japan). The Ethical Review

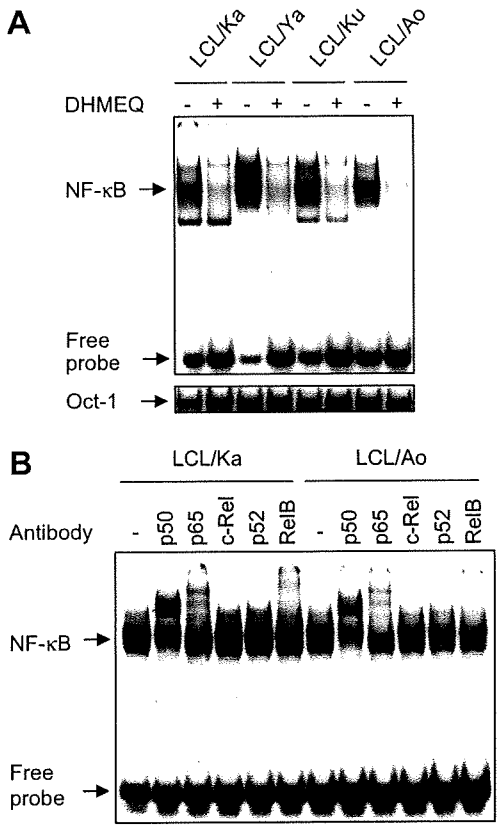

Fig. 1. Inhibition of constitutive NF-κB binding activity in LCLs by DHMEQ. (A) Inhibition of constitutive NF-κB activity in LCLs. LCLs were treated with 10 μg/ml of DHMEQ (+) or with DMSO alone (−) for 3 h. Nuclear extracts (2.5 μg) were examined for NF-κB binding activity by electrophoretic mobility shift analysis (EMSA) with a radiolabeled NF-κB-specific probe. Binding of Oct-1 served as a control. (B) Subcomponents of constitutive NF-κB activity in LCLs. Nuclear extracts (1 μg) of cells without DHMEQ treatment were subjected to supershift analysis with antibodies specific for NF-κB p50, p65, c-Rel, p52, and RelB or without antibody (−). The experiment using isotype matched IgG control showed the same result (data not shown). The position of shifted bands corresponding to NF-κB and free probes are indicated on the left.

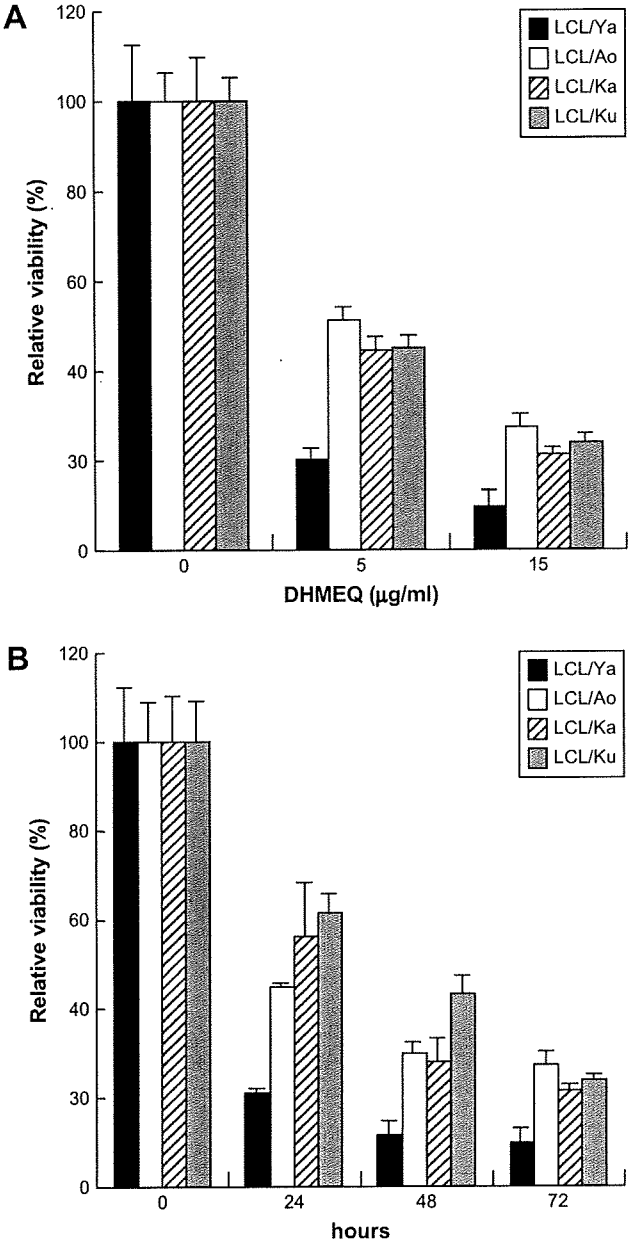

Fig. 2. DHMEQ inhibits proliferation of LCLs. The viability of the cells was determined by WST-8 assay and the relative levels compared with those of DMSO-treated cells are presented. Data represent the mean and standard deviation of triplicate experiments. (A) Results of dose–response experiments. LCLs were treated with 0, 5, or 10 μg/ml of DHMEQ for 72 h. ALL LCLs treated with 0, 5, or 10 μg/ml of DHMEQ showed statistical significance compared to DMSO-treated controls. (B) Results of time–response experiments. LCLs were treated with 10 μg/ml of DHMEQ for 24, 48, and 72 h. ALL LCLs treated for 24, 48, and 72 h except for LCL/Ku at the point of 24 h showed statistical significance compared to DMSO-treated controls.

Committee of the National Institute of Infectious Diseases approved the experimental protocol. 1×10^6 LCL cells were inoculated subcutaneously into the post-auricular region of NOG mice. DHMEQ was administered three times a week for 1 month into the post-auricular region of mice at a dose of 12 mg/kg, beginning on day 5 when tumors were palpable. The control mice were injected RPMI-1640 as was performed in our recent published papers [15,16]. Mice were killed 1 month after inoculation.

2.7. Immunohistochemistry

Cells were immunostained with antibodies and fluorescence signals were detected using confocal microscopy. Cytospin samples were prepared using 5×10^5 cells and cells were first washed three times with phosphate-buffered saline (PBS). Cells were then fixed with 100% cold acetone for 10 min at room temperature and washed three times in PBS. Samples were incubated with primary antibody at the concentration

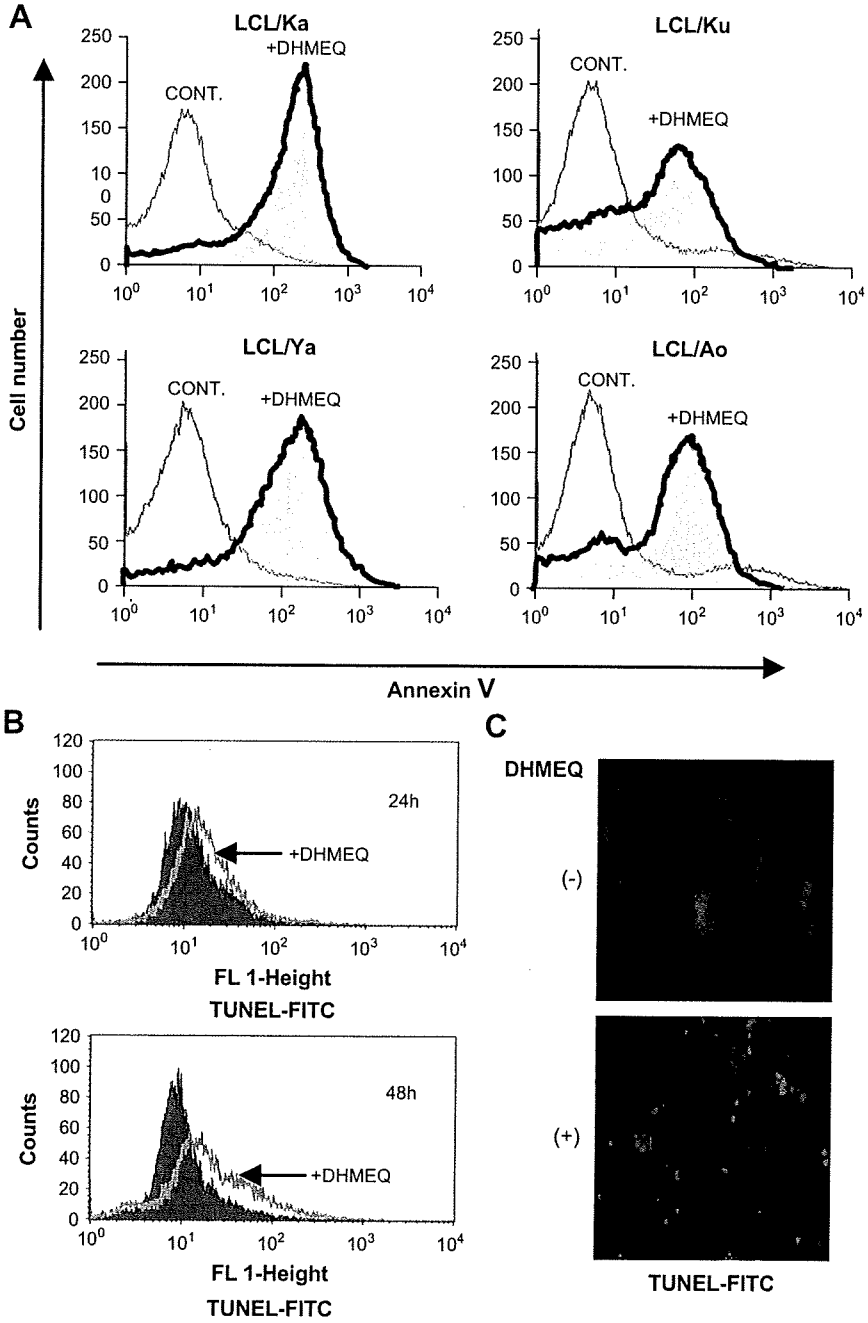

Fig. 3. DHMEQ induces apoptosis in LCLs. (A) Annexin V reactivity in LCLs after DHMEQ treatment. LCLs were treated with (filled curve) or without (open curve) 10 μg/ml of DHMEQ for 48 h, and the binding of FITC-conjugated Annexin V was analyzed by flow cytometry. (B) DNA fragmentation in LCL cells after DHMEQ treatment. DNA fragmentation in LCL cells was detected by TUNEL assay with flow cytometry. Representative flow cytometric profiles are shown for cells treated with 10 μg/ml of DHMEQ (open curve) or with DMSO alone (filled curve) for 24 h (upper panel) or 48 h (lower panel). (C) LCL cells were treated with 10 μg/ml of DHMEQ (+) or with DMSO alone (−) for 48 h, fixed on slides, and processed for TUNEL assay. A filter that selectively detects fluorescein isothiocyanate (FITC)-TUNEL fluorescence was used for the microscopic observation.

of 5 μg/ml at 4 °C overnight and washed with PBS three times. After incubation with fluorescence-labeled secondary antibody for 30 min at 37 °C, samples were washed three times in PBS and covered with a Perma Fluoro antifade reagent (Therme Shandon Co., Pittsburgh, PA). Fluorescence signals were detected using confocal microscopy (Radiance 2000) (Bio-Rad Laboratories. Antibodies used were as follows: anti-Epstein–Barr virus LMP clones CS, 1-4 mouse monoclonal antibody (Dako, Kyoto, Japan), and anti-p65 (c-20) goat polyclonal antibody (Santa Cruz Biotechnology Inc.

2.8. Real-time quantitative PCR

The expression level of anti-apoptotic genes was quantified by real-time reverse transcription–polymerase chain reaction (RT–PCR). Total RNA was extracted from the cells by ISOGEN reagent (Nippon Gene Co., Toyama, Japan) and treated according to the manufacturer's instructions. cDNA was synthesized using oligo dT and random primers synthesized with a PrimeScript RT reagent kit (Takara Bio Inc., Shiga, Japan). Amplification was performed with SYBR premix Ex Taq (Takara Bio Inc.) and the primer sets for c-IAP1, Bfl-1, BCL-XL, and c-FLIP (Takara Bio Inc.). The viral DNA load in EBV-infected PBMC was determined by real-time PCR with slight modifications of a previously described method [17]. DNA samples were extracted from the cells with a DNeasy tissue kit (Qiagen, Hilden, Germany). Amplification with SYBR premix Ex Taq (Takara Bio Inc.) and primers for BALF5 gene encoding the viral DNA polymerase (5′-CGG AAG CCC TCT GGA CTT C-3′ and 5′-CCC TGT TTA TCC GAT GGA ATG-3′) was performed using the Thermal Cycler Dice Real Time System (Takara Bio Inc.) and analyzed using the manufacturer's software.

2.9. Statistical analysis

Differences between mean values were assessed by *t*-test. A *P*-value of <0.05 was considered to be statistically significant.

3. Results

3.1. DHMEQ efficiently blocks constitutive NF-κB activity in LCLs

We first examined the effects of DHMEQ against constitutive NF-κB activity in established LCLs. Treatment with DHMEQ at a concentration of 10 μg/ml abrogated constitutive NF-κB binding activity in these cell lines (Fig. 1A). Components of NF-κB that are constitutively activated in LCLs were analyzed by

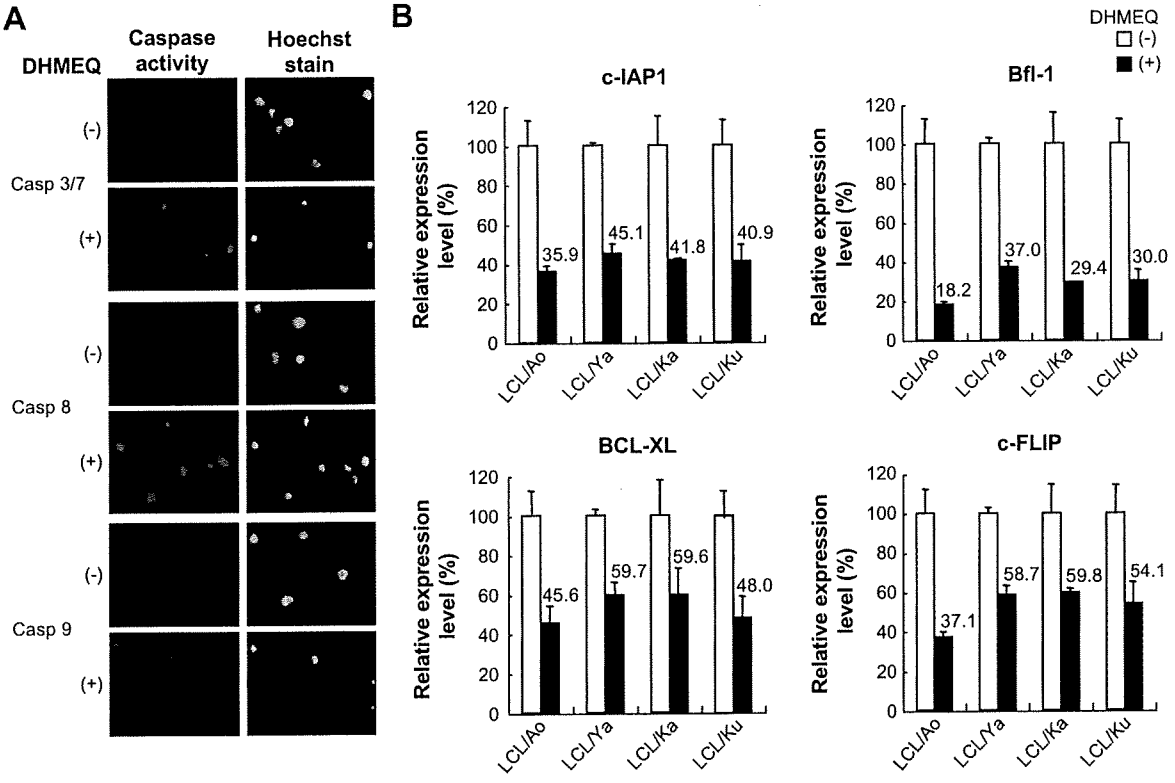

Fig. 4. Activation of caspase-3, -8, and -9. (A) LCL cells were treated with 10 μg/ml of DHMEQ (+) or with DMSO alone (−) for 8 h and fixed on slides. Caspase-3/7, -8, and -9 activities in LCLs after DHMEQ treatment were detected by green fluorochrome-labeled inhibitors of caspases (FLICA)-3/7, -8, and -9 (left panels) and nuclear DNA was stained with Hoechst 33342 (right panels). (B) Effects of DHMEQ on genes regulating apoptosis in LCLs. Quantification of the gene expression by real-time PCR. LCLs were treated with 10 μg/ml of DHMEQ (+) or with DMSO alone (−) for 4 h. The expressions of c-IAP1, Bfl-1, BCL-XL, and c-FLIP were quantified by real-time PCR. The data are means with standard deviation of triplicate experiments. The numbers above the bar graphs indicate the means of each gene expression after DHMEQ treatment. The reduction of the expressions of c-IAP1, Bfl-1, BCL-XL, and c-FLIP was statistically significant.